



# Investigation of the ground movement due to underground mining at the Jinshandian Iron Mine in China

Kaizong Xia<sup>1</sup> · Congxin Chen<sup>1</sup> · Zude Lu<sup>1</sup> · Kuoyu Yang<sup>1,2</sup> · Yun Zheng<sup>1</sup> · Hansong Pang<sup>1,2</sup> · Chaoyi Sun<sup>1,2</sup>

Received: 9 June 2019 / Accepted: 27 November 2019 / Published online: 6 December 2019  
© Springer-Verlag GmbH Germany, part of Springer Nature 2019

## Abstract

To investigate the mechanism responsible for mining-induced ground movement at the Jinshandian Iron Mine in China, the vertical and horizontal deformations of the ground-surface were monitored in situ over a period of 8 years. The results were analyzed and combined with subsidence results derived from laser-scanning measurements and collapse/cracking behavior of the ground. The results show that the horizontal displacement mainly occurs in the rock masses surrounding the mined voids. Moreover, several obvious onset points can be found in the displacement–time curves that are indicative of rapid increases in displacement. Currently, the scope of the ground movement of the footwall is larger than that of the hanging wall. This behavior is distinctive and distinguishes the Jinshandian Iron Mine from others. It can be attributed to the sliding–toppling failure of the column-shaped rock masses in the footwall under the combined effect of the in situ horizontal stress and high dip angles of the discontinuities.

**Keywords** Underground mining · Sublevel caving · Ground movement · Movement and break angles · Horizontal stress · Discontinuity

## Introduction

The demand for mineral resources has increased dramatically in recent years due to a rapid development in human social and economic activity. To meet this demand, more and more metal mines are tending to move towards large-scale underground mining, wherein the depth and scope of the orebodies being extracted are being continuously extended. However, various environmental problems have arisen as a result, and deformation and movement of the ground in the mining area are of particular concern (John and Lupo 1997; Reid 1998; Hebblewhite 2001; Bruneau et al. 2003a, b; Villegas et al. 2011; Edelbro et al. 2012; Svartsjaern et al. 2016;

Xia et al. 2016, 2019; Cheng et al. 2017a, b; Wang et al. 2019). Thus, there is a need to protect nearby buildings and facilities at the ground-surface, and this requirement forms the basis for the design of the mining installations and their safe operation.

Revealing the mechanisms by which the mining of large-scale orebodies can induce ground movement has thus become a pressing issue. Researchers have conducted various studies related to ground movement. Reid (1998), Hebblewhite (2001) and Xia et al. (2016) found that localized horizontal movement could be observed at large distances away from the boundaries of voids mined in metal mines (in contrast, the vertical deformation observed in these areas is negligible). Bruneau et al. (2003a, b) investigated the effect of major geological structures (e.g., faults) on the stability of the main mine shaft, and found that there is a zone of tension around the shaft that results in vertical displacement. John and Lupo (1997), Villegas et al. (2011), Edelbro et al. (2012) and Svartsjaern et al. (2016) reported that the surface of the ground at the Kiirunavaara Mine in Sweden had been subjected to large-scale deformation and cracking since sublevel caving (SLC) had been implemented, and that two general types of deformation zone could be observed (discontinuous and continuous). Based on the geological features of

✉ Kaizong Xia  
kzxia@whrsm.ac.cn

✉ Kuoyu Yang  
yangkuoyu16@mails.ucas.ac.cn

<sup>1</sup> State Key Laboratory of Geomechanics and Geotechnical Engineering, Institute of Rock and Soil Mechanics, Chinese Academy of Sciences, Wuhan 430071, Hubei, People's Republic of China

<sup>2</sup> University of Chinese Academy of Sciences, Beijing 100049, People's Republic of China

the footwall in the Chengchao Iron-ore Mine, Cheng et al. (2017a), Xia et al. (2017) and Song et al. (2018) suggested that rock masses under the action of high horizontal stress can be represented using a simplified analytical mechanical model in the form of a cantilever beam. Li et al. (2004), Zhao et al. (2013), Ma et al. (2015) and Ding et al. (2018) reported that although the mining method adopted in the Jinchuan Nickel Mine is based on the 'cut-and-fill' technique, ground-surface deformation and movement could still be readily observed via field and ground-surface deformation-monitoring investigations.

In general, the evaluation of subsidence in a mining area mainly depends upon the geological context (e.g., the faults, joints, and in situ stress), and so the geological factors affecting the scope of the ground movement in metal mines are quite complex. As a result, the ground movement associated with the removal of underground orebodies is an extremely complex mechanical process. Currently, the mechanical-extension mechanism underpinning the ground movement in metal mines has not been studied in great depth because of the complex geological conditions present. Moreover, no model or method has been proposed to fully evaluate the scope of the ground movement in different geological conditions. In fact, the investigation into the extension mechanism responsible for ground movement induced by the excavation of underground orebodies is still in its initial stages for metal mines. More importantly, due to the fact that metal mines are frequently subjected to many strong tectonic events, before and after the formation of the orebody, large in situ horizontal stress often exists within the surrounding rock masses. In addition, this stress is usually larger than the vertical stress caused by gravity (Cai et al. 2000; Li et al. 2004; Xia et al. 2016; Cheng et al. 2017a; Ding et al. 2018). Thus, a large in situ horizontal stress field can significantly affect the behavior of the ground with respect to movement. Consequently, the surrounding rock mass is often subjected to large-scale ground movement earlier than expected. As a result, the scope of the land expropriated may be too small and this can cause serious losses to the economy, society and environment.

The Jinshandian Iron Mine is a typical example of the metallic mines found in China. It has a mining area of approximately 3.5 km<sup>2</sup> and an annual output of 3,000,000 tons of iron ore. Based on the design requirements, the SLC mining method without sill pillars is adopted in this mine. This is a widely-used mining method that utilizes gravity to encourage the flow of blasted ore and caved waste rock (Brady and Brown 2006; Xia et al. 2019). That is, the orebody is fragmented by blasting and the overlying host rock fractures and caves under the stress induced by mining activity and gravity (Brunton et al. 2010). Thus, the mined voids are filled by the caved rock masses which help to control the ground pressure. As a large-scale, privately

mined-out area was present in the upper part of the overlying strata in the Jinshandian Iron Mine, the collapse of ground surface above the privately mined-out area occurred before the initial mining sublevel had been completed in April 2007 due to the disturbance created by the excavation of the underground orebody. Subsequently, a large number of local residents were forced to evacuate. After the private pit collapsed, the movement of the ground rapidly extended outwards as the mining depth increased. As a result, the foundations of many buildings and facilities ended up within the area of movement, e.g., railways, drainage ditches, back-fill station (which was completed but never used), and eastern ventilation shaft.

Currently, the scope of the ground movement in the footwall is significantly larger than that designed in the initial mining stage. The buildings and facilities in this area have been subjected to large-scale deformation and cracking much earlier than expected and this has become a major problem for the safe operation of the Jinshandian Iron Mine. Interestingly, by analyzing the monitoring data and the characteristics of the collapsing and cracking behavior of the ground surface in this mine, some distinctive features concerning the ground movement can be found compared to other metal mines.

To investigate the mining-induced ground movement occurring near the Jinshandian Iron Mine in China, in situ monitoring investigations were carried out over an 8-year period to determine the vertical and horizontal ground-surface deformations experienced. The results were then analyzed and combined with subsidence results obtained using a laser-scanning method and collapse/cracking behavior of the ground-surface. The combined results were used to investigate the mechanism responsible for the mining-induced ground movement in this mine.

The main objectives of this paper are: (i) to analyze the characteristics of the ground-surface deformation and movement induced by underground orebody excavation, and determine the characteristics of the scope of the ground movement; (ii) to investigate the mechanism responsible for the mechanical extension of the ground in the footwall under the combined effect of the in situ horizontal stress and high dip angles of the discontinuities; (iii) to elucidate the reason why the surrounding rock masses in the footwall were subjected to large-scale ground movement earlier than expected.

## Mine site investigation

### Strata lithology

The metalliferous deposits available in the Jinshandian Iron Mine lie in a complex topographical environment. There is the presence of either mountains or hills, and

the mining area is divided into eastern and western parts by exploration line 25. The eastern part ranges from line 25 to 43 making it about 1000 m long and 570 m wide. It is mainly comprised of orebodies I and II (Figs. 1 and 2). The lithology of the mining area features a sandstone–shale mixed stratum of the Middle–Upper series of the Triassic System, and magmatite from the Middle–Late age of the Yanshan Movement. The sandstone–shale mixed stratum is distributed in the hanging wall of the orebody and the magmatite constitutes the footwall rock of the orebody. The magmatite mainly consists of quartz diorite (as well as diorite, gabbro diorite, dioritic porphyrite, and diabase porphyrite). In addition, a small amount of limestone from the Middle series of the Triassic System can be found in the mining area. Under the effect of the thermal and metasomatism metamorphism that occurred during magmatite intrusion, the sandstone–shale was metamorphosed into various hornstones (argillaceous hornstone, quartz-feldspar hornstone, argillaceous biotite hornstone, blasto-siltstone, blasto-psammite, etc.)—the limestone was metamorphosed into marble. The bedding surface for the strike of the hornstone lies in an approximately E–W

direction and is oriented at  $174^{\circ}\text{--}186^{\circ} < 62^{\circ}\text{--}84^{\circ}$ . Marble forms the main overburden strata of orebody II, and is mostly distributed between the hornstone and magmatite. In addition, the overburden Quaternary layer mainly consists of tawny or grey residual clays and clayish gravels, and is widely distributed throughout the entire mining area. It has a maximum thickness of 20 m, and so bedrock outcrops are rarely observed on the surface of the ground.

For these kinds of hornstone, significant differences in strength are encountered when they are in altered or weathered states (Table 1). The intact rock strength of the magmatite is extremely high, to the extent that the unconfined compressive strength may reach up to 200 MPa. However, the strength of the magmatite is also degraded when it is weathered and altered (Table 2). Specimens of quartz diorite were taken from the rock mass near the orebodies and, therefore, were not intact and had a high degree of alteration. Thus, their uniaxial compressive strengths were relatively low. However, only a small difference in uniaxial compressive strength was found between the quartz diorite and the hornstone.

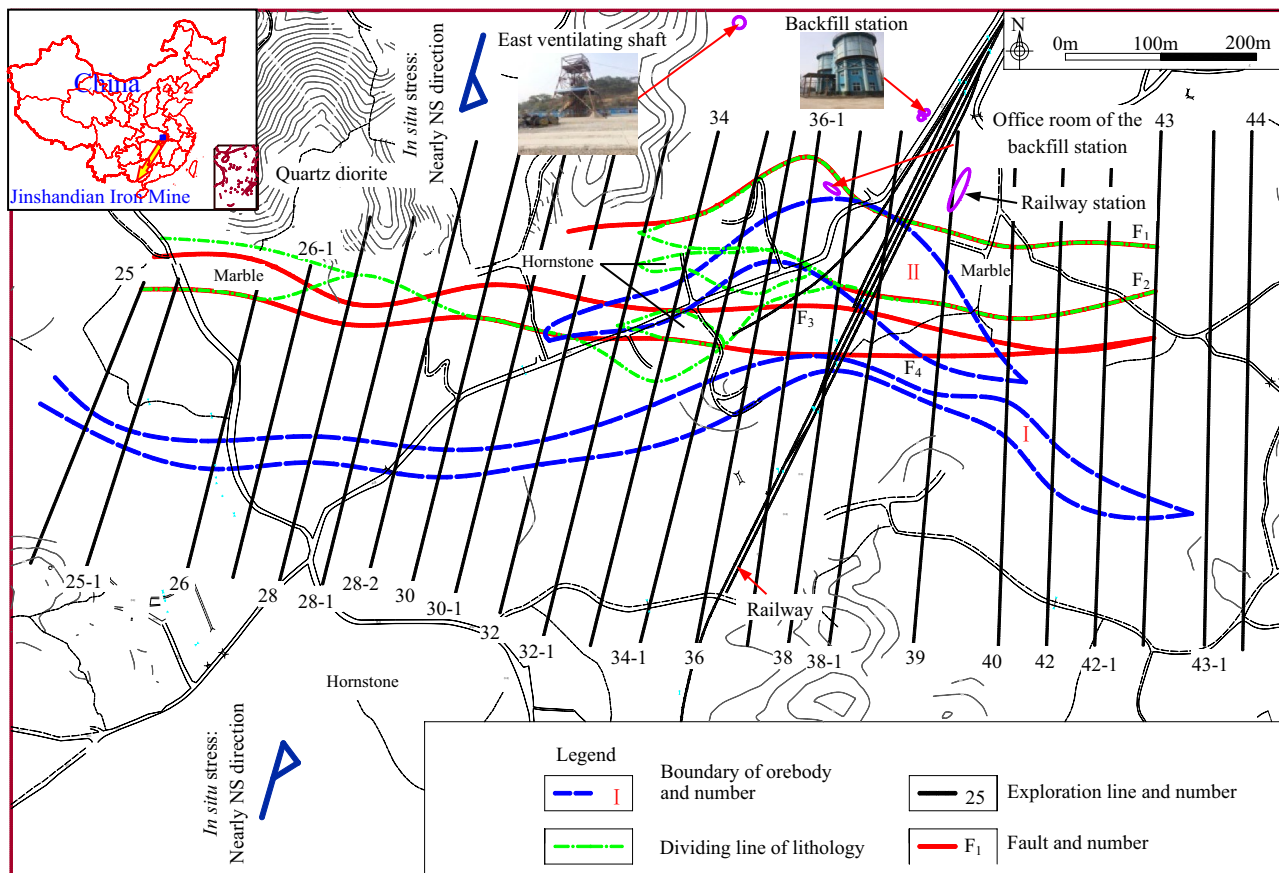


Fig. 1 Key facility, orebody (– 410 m) and fault distributions in study area

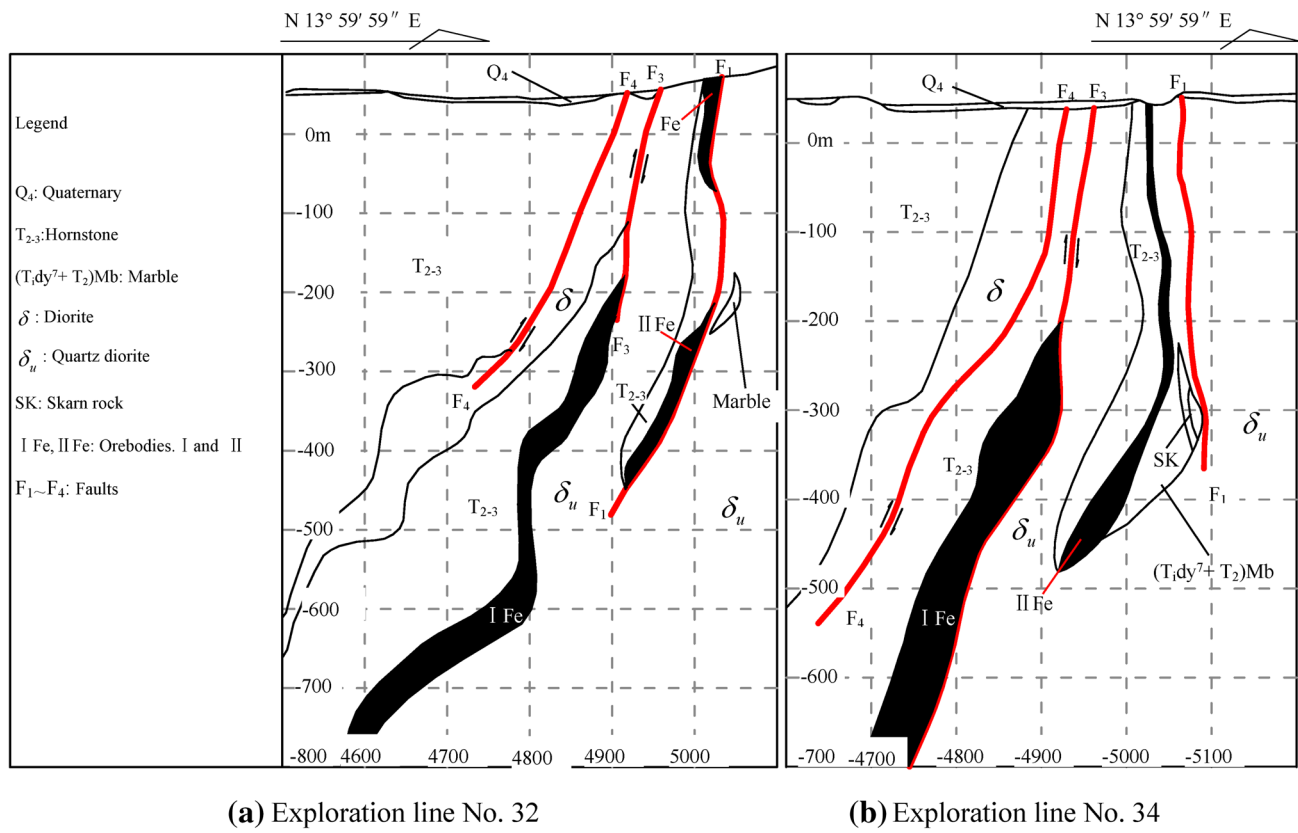


Fig. 2 Typical geological profiles

Table 1 Uniaxial compressive strength of the hornstone

Lithology	Surface conditions and structures	Uniaxial compressive strength (MPa)		
		Maximum	Minimum	Mean average
Argillaceous hornstone	① Slightly weathered to fresh, non- to weakly-altered, intact	> 175	100	125
	② Moderately to slightly weathered, weakly to moderately altered, relatively intact	95	64	72
	③ Moderately to slightly weathered, moderately to highly altered, with spaced discontinuities.	57	13	34
Blasto-psammite	Above ①	> 175	135	150
	Above ②	123	98	112
	Above ③	33	21	29
Blasto-siltstone	Above ①	> 175	114	158
	Above ②	119	56	95
	Above ③	64	13	39
Argillaceous biotite hornstone	Above ①	165	93	125
	Above ②	106	53	67
	Highly altered and fractured	74	15	36



**Table 2** Uniaxial compressive strength of the magmatite (from point load testing)

Lithology	Surface conditions and structures	Number of specimens	Uniaxial compressive strength (MPa)		
			Maximum	Minimum	Mean average
Quartz diorite	Most rock specimens are moderately to slightly weathered, weakly to highly altered, with the obvious discontinuity surfaces and hidden fissures	30	153	20	72
Diorite	Moderately weathered, highly altered, with an obvious discontinuity surface and hidden fissures	15	110	18	79
Gabbro diorite	Slightly weathered, moderately altered, relatively intact	6	149	67	105
Dioritic porphyrite	Slightly weathered, weakly altered	9	174	78	123
Diabase porphyrite	Fresh, weakly to moderately altered	8	108	28	74

## Rock mass structure

Four subparallel faults with strikes in an approximate E–W direction are found in the mining area (see Figs. 1 and 2). Their features can be summarized as follows:

- (1) Fault  $F_1$ : distributed to the east of exploration line 32 with a strike in an approximate E–W direction and length of about 1500 m. The fracture zone of this fault is quite developed, and its width ranges from 15 to 35 m at ground level.
- (2) Fault  $F_2$ : distributed to the east of exploration line 38 with a strike ranging from E–W to N 80° W (and dipping direction ranging from N–S to S 10° W). The dipping angle of the fault gradually decreases from 85° to 55° as depth increases, and its fracture zone is also quite developed.
- (3) Fault  $F_3$ : distributed throughout the entire mining area with an approximate strike of N 84° W (and dipping direction ranging from S 6° W). It is located in, or near, the contact zone between the hornstone and magmatite layers. The dipping angle of this fault gradually decreases from 87° to 55° as depth increases. Its fracture zone is quite developed with a width that ranges from 15 to 35 m at ground level.
- (4) Fault  $F_4$ : distributed throughout the entire mining area subparallel to  $F_3$ . It is located within the hornstone layers. The dipping angle of the fault gradually decreases from 85° to 55° as depth increases. The fracture zone of the fault is quite developed and its width ranges from 10 to 35 m at ground level.

A field investigation was conducted to ascertain the state of development of the major discontinuities in this mine based on some well-developed geological outcrops. These outcrops included those at the ground-surface, the main roadways of the – 340, – 354, – 368, – 382 and – 396 m mining levels, and part of the unsupported transverse drift roadway. Based on the results obtained, rose diagrams and

stereographic projections were then drawn for the discontinuities in the hanging wall (hornstone) and footwall (mainly quartz diorite), as presented in Fig. 3. Important information pertaining to the major discontinuities is also summarized in Table 3.

Table 3 shows that five groups of major discontinuities are to be found in the quartz diorite of the footwall each with high persistence. Most of the discontinuity surfaces are closed or slightly open (width < 3 mm) and are smooth or locally rough. They show characteristics typical of shear behavior, and a small number of them are filled with carbonate or skarn. Three groups of major discontinuities are to be found in the hanging wall, the surface features of which are similar to those of the discontinuity surfaces within the quartz diorite. Laboratory tests were also carried out to determine the characteristics of the discontinuity surfaces in the mining area. The mechanical parameters of the discontinuity surfaces thus found are illustrated in Tables 4 and 5.

## In situ stress field

Two measurements of the in situ stress in the marble ( $\pm 0$  m) and diorite (– 250 m) of the footwall of the Jinshangdian Iron Mine were undertaken (Table 6).

The results obtained for the marble ( $\pm 0$  m) clearly show that the major principal stress ( $\sigma_1$ ) is 9.84 MPa and that the gravitational stress at this depth is 1.56 MPa. The corresponding measurements in the diorite (– 250 m) yield a major principal stress of 15.79 MPa (with azimuth N 16.26° E), and a gravitational stress of 9.28 MPa. The in situ stress field cannot be accurately characterized using just two measurements. However, the way the in situ stress changes with depth can be roughly predicted in general. That is, the in situ stress generally increases with depth (Xu 2007), and most of the metal mines in China have this characteristic, e.g., the Meishan iron mine, Jinchuan Nickel Mine and Shuichang iron mine (Cai et al. 2000; Li et al. 2004; Tan et al. 2014; Ding et al. 2018). Although only two measurements were made in this study, the results obtained are consistent with

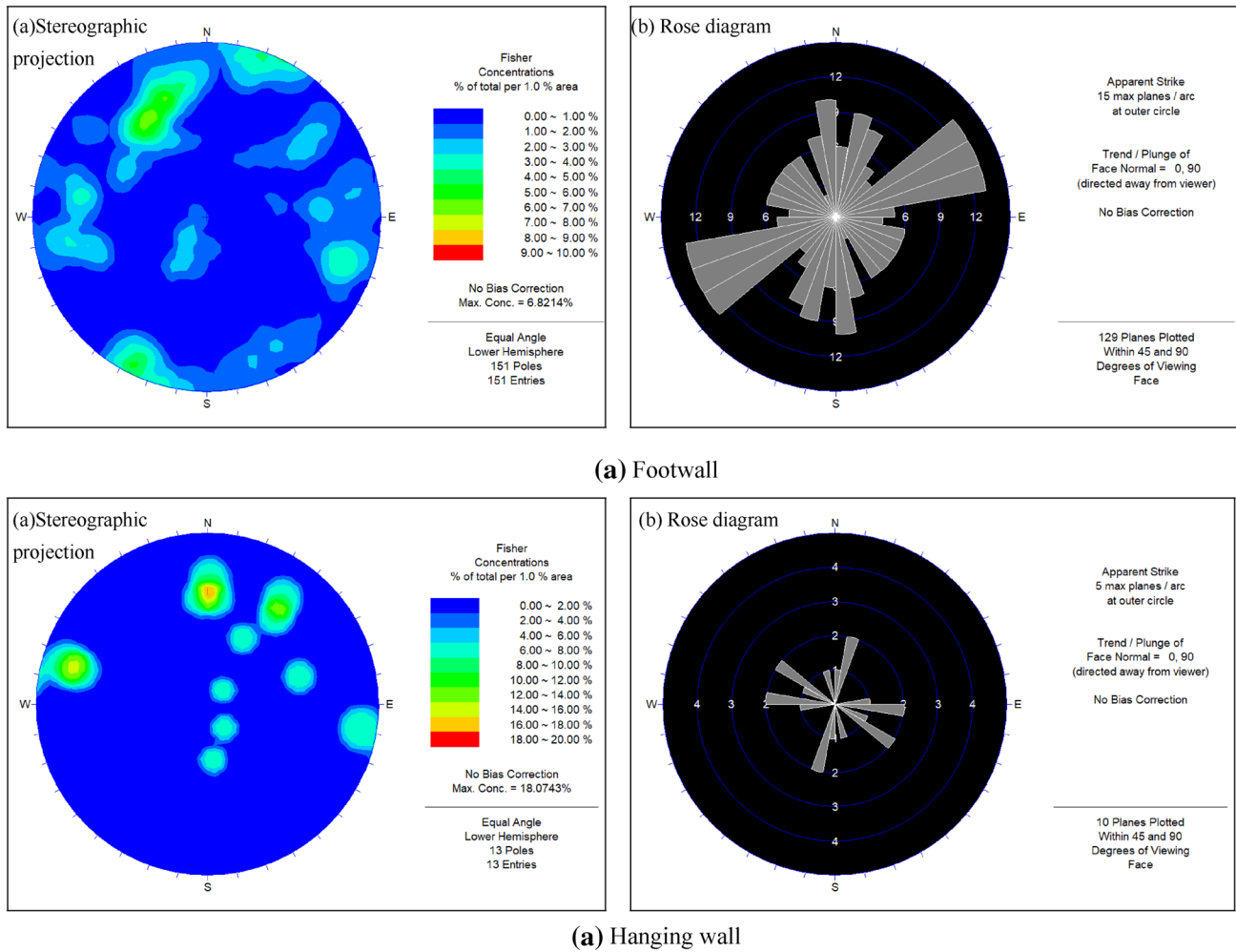


Fig. 3 Rose diagrams and stereographic projections for the discontinuities in the hanging wall (hornstone) and footwall (mainly quartz diorite)

Table 3 Discontinuities in the rock surrounding the mine

No.	The attitude of the major discontinuity in the footwall				No.	The attitude of the major discontinuity in the hanging wall			
	Range value		Orientation	Spacing (m)		Range value		Orientation	Spacing (m)
	Dip direction (°)	Dip angle (°)				Dip direction (°)	Dip angle (°)		
1	135–178	50–83	156° < 68°	0.32	1	176–185	63–73	181° < 66°	0.30
2	2–31	66–89	20° < 84°	0.50	2	215–218	65–74	217° < 70°	
3	194–211	74–87	200° < 83°	0.70	3	105–106	75–81	106° < 78°	
4	279–296	60–85	287° < 76°	0.63					
5	70–85	64–82	77° < 74°	0.35					

the general case, i.e., the stress in a mining area of greater depth is higher than that at the surface.

To further verify this conclusion, the in situ stresses measured in a metal mine near the Jinshangdian Iron Mine were collected. These results indicated that:  $\sigma_1 = 1.9 + 0.08H$  MPa and  $\sigma_2 = -0.12 + 0.07H$  MPa,

where  $H$  is the thickness of the overburden strata in meters. Hence, the in situ stress in this metal mine certainly increases with depth, which supports the above conclusion. Comparing the major principal stress in these two metal mines with the gravitational stress shows that the major principal stress is larger than the vertical stress

**Table 4** Shear strength parameters of the discontinuity surface

Lithology	Peak shear strength		Residual shear strength	
	Cohesive (c) (MPa)	Internal friction angle ( $\phi$ )	Cohesive (c) (MPa)	Internal friction angle ( $\phi$ )
Quartz diorite	0.182	35° 49'	0.052	36° 24'
Hornstone	0.211	21° 18'	0.341	15° 35'

The discontinuity surface is taken from – 270 m mining level

**Table 5** Shear strength parameters of the discontinuity surface within quartz diorite under saturated conditions

Peak shear strength		Residual shear strength	
Cohesive (c) (MPa)	Internal friction angle ( $\phi$ )	Cohesive (c) (MPa)	Internal friction angle ( $\phi$ )
0.087–0.207	19° 23'–36° 24'	0.012–0.138	18° 00'–35° 27'
0.154/8	26° 20'/8	0.044/8	25° 28'/8

In this table, the numerator is the average value of the testing results, and the denominator is the number of the tested rock specimens

**Table 6** Measured in situ stress in the western mining area

± 0 m level (ground elevation 60 m)			– 250 m level (ground elevation 107 m)	
In situ stress	Value (MPa)	Azimuth	Value (MPa)	Azimuth
$\sigma_1$	9.84	245.74°	15.79	196.26°
$\sigma_2$	4.48	133.90°	4.79	304.78°
$\sigma_3$	0.50	194.32°	0.48	39.28°
Geostatic	1.56		9.28	

caused by gravity (generally it is one to two times higher). Therefore, there exists a significant tectonic stress field in the Jinshandian Iron-ore Mine, which will surely exert a significant effect on the movement of the ground. Furthermore, the major principal stress in the surrounding rock masses lies in an approximately NNE to SSW direction.

**Description of the mined-out areas**

Following the local design requirements of the SLC method (without sill pillars), the phase height is 70 m, sublevel interval 14 m and cross-cut drift spacing 16 m. The orebodies that had been excavated out to December 2016 include the levels at – 270, – 284, – 298, – 312 and – 326 m. The beginning (end) dates and planar projections associated with these mined-out areas are shown in Table 7 and Fig. 4, respectively. By December 2016, the orebodies in the –340 m sublevel had been generally excavated out, and two-thirds of orebody I in the – 354 m sublevel had also been

**Table 7** Mining situations

Mining level (m)	Mining date	
	Start	End
– 270	Feb. 2007	May 2009
– 284	Dec 2007	Dec 2012
– 298	Mar 2012	Orebody No. I: Sept 2013; orebody No. II: Jun 2014
– 312	Orebody No. I: Dec 2012; orebody No. II: Apr 2012	Nov 2014
– 326	Orebody No. I: May 2014; orebody No. II: Dec 2014	Mar 2016
– 340	Mar 2015	–
– 354	Orebody No. I: Dec 2015	–

excavated out. It should be noted that, during the mining of the – 284 m sublevel, excavation activity in the orebodies was forced to stop (from April 2009 to March 2012) because an issue relating to compensation (for resident relocation) remained unresolved.

In addition to this activity, large-scale private mining was carried out in the initial mining stage—the relevant shaft locations are shown in Fig. 5. The existing data indicate that the privately excavated mines reached a depth corresponding to an elevation of approximately – 160 m, and the ore recovered amounted to ~1,000,000 tons. The results of seismic detection indicate that the planar distributions of the privately mined-out areas and fractured areas are shown in Fig. 5.

**Ground collapse and cracking**

**Ground surface collapse**

As discussed above, as large-scale privately-mined voids are widely distributed in the upper parts of the overlying strata, further excavation of the underlying orebodies will have a significant effect on the stability of the privately mined-out areas. Thus, in April 2007 (before the initial sublevel had been completely mined), the surface of the ground collapsed near private mining location 2 without pre-warning (see Fig. 6). An area of about 250 m<sup>2</sup> collapsed, and this caused cracking in three buildings around the collapsed pit.

Similarly, in September 2008, the ground collapsed near private mining location 3 with a collapse area of approximately 620 m<sup>2</sup>. Thereafter, with the mining activity extending deeper and deeper, there was large-scale caving-in of the overlying strata above the mined-out areas which

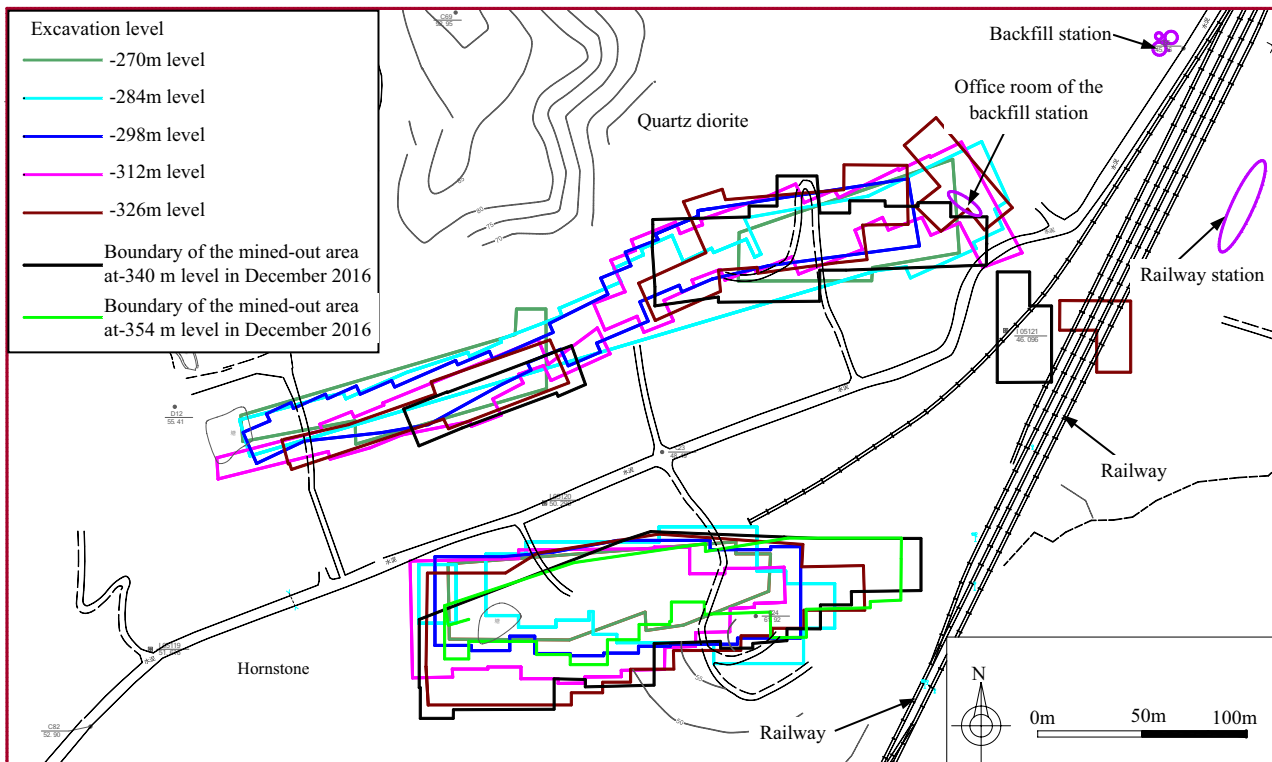


**Fig. 4** Planar projection of the mined-out areas

extended to the ground level. In February 2013 and May 2013, large-scale ground-surface collapse again occurred near the privately mined-out areas (No. 3 and 2, respectively, see Fig. 7a, b), and some fresh soil could be seen on the surfaces of these collapsing pits. After this, the scope of the collapse continued to extend outwards as the mining activity extended to greater depths. In addition, many new, smaller collapses frequently occurred in the ground surface, especially near the collapsed pit above the mined-out areas created by the extraction of orebody II (i.e., the northern mined-out area). Currently, the northern and southern collapses have joined together forming a larger collapse pit.

### Ground surface cracking

With the mining activities extending to greater depth, two field investigations of the ground surface cracks were specifically conducted in December 2014 (after ground surface collapse) and in December 2016 (Fig. 6): in the hanging wall, only a few ground surface cracks with a scattered spatial distribution were observed near the boundary of the mined voids (the maximum distance was about 80 m to the mined-out areas, see Fig. 8d), and their widths mostly range from 40 to 80 cm. However, in the footwall, many large ground surface cracks with significant dislocation and opening can

be found (Fig. 8a, b, c), and the dislocation displacement can reach approximately 2.0 m.

In these areas, two major cracks of length ~ 130 m can be found that intersect with the drainage ditch (Figs. 6 and 8b). Their strikes approximately lie in the direction N 70° W, and their dislocation and opening displacements amount to 2.0 m and 1.5 m, respectively. Meanwhile, a branched major crack was found in the western area near the mined-out region (with a strike of approximately N 30° E and length of about 80 m). Outside the branched major crack, a major crack was to be found with a length of about 100 m and dislocation and opening displacements that are both about 1.5 m (Figs. 6 and 8c). Its strike is generally parallel to the branched major crack. Moreover, the outermost major cracks are approximately 100 m from the boundary of the mined-out areas in the footwall. Regardless of the cracks in the hanging wall and those in the footwall, these cracks mostly show evident shearing behavior.

In many mining-affected areas it is often hard to find cracks in the ground surface. However, in this case, it was easy to see cracks in concrete pavements, brick-concrete structural facilities and buildings (see Fig. 8e–h). In general, these cracks are mostly ranged from 1 to 3 cm wide. More specifically, at ~ 50 m away from the east ventilating shaft, the widths of the cracks in the drainage ditch are of the order of 2 cm (Fig. 8e),

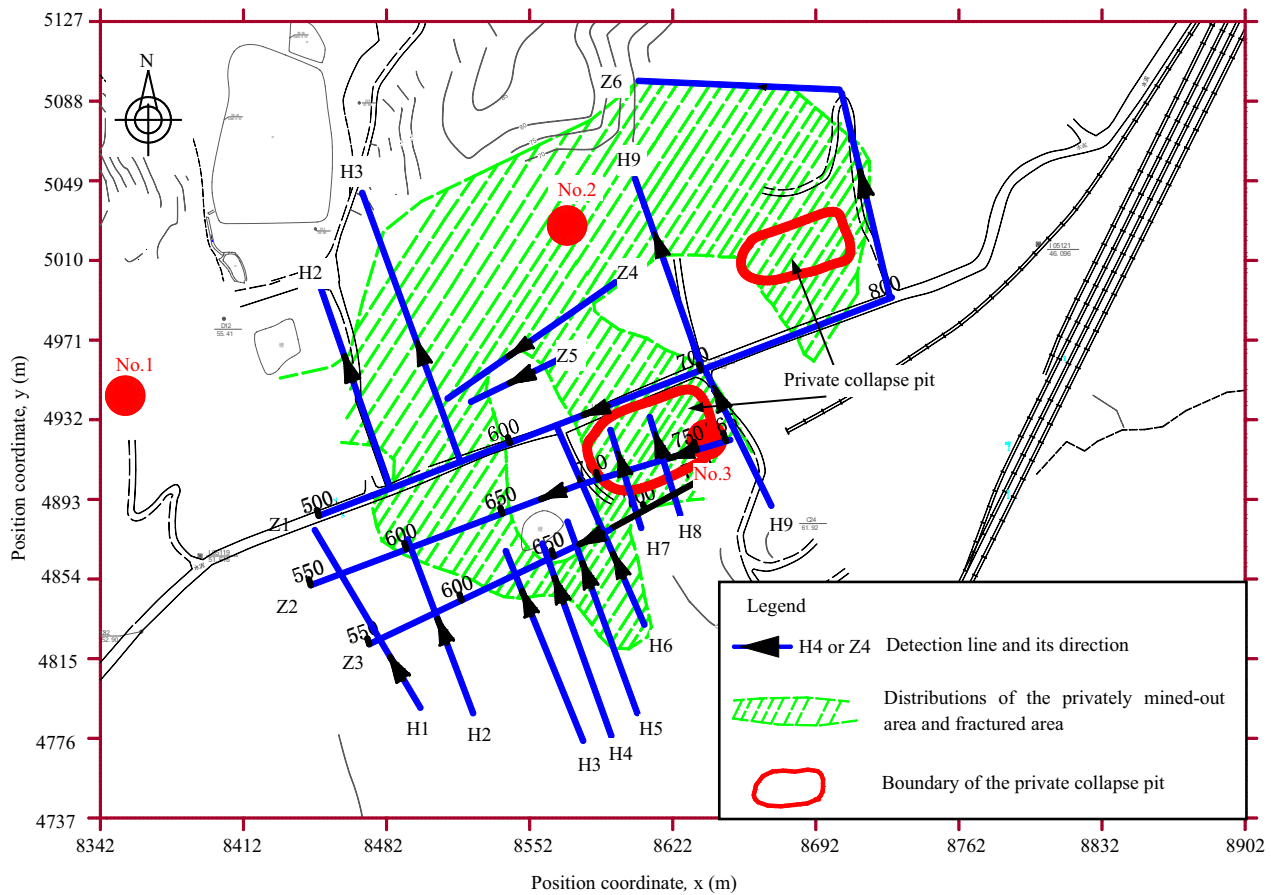


**Fig. 5** Planar distributions of the privately mined-out area and fractured area based on the seismic detection results (the No. 1 to 3 refer to the shaft location of the private mining)

and the width of the crack in the subsidiary building of the backfill station is approximately 1.5 cm (Fig. 8f).

### Analysis of the ground deformation

#### Methodology

After the private pit collapsed, GPS monitoring was introduced to the mining-affected area considering the complex topographical environment surrounding the mine to investigate the mining-induced ground surface deformation (Mancini et al. 2009; Ng et al. 2010; Villegas et al. 2011; Liu et al. 2012; Villegas and Nordlund 2012; Can et al. 2013; Ma et al. 2015; Cheng et al. 2017a). To fully cover the scope of the mining-affected area, a monitoring network consisting of two reference points and 55 deformation monitoring points was established in April 2008 (Fig. 9a). The data from these monitoring points were recorded using a static approach, and measurements made once a month before March 2015, and bimonthly thereafter. During the measurement process, two

GPS instruments remained fixed at the two reference points. These were located on stable ground far away from any excavation-influenced areas. The other GPS instruments were arranged at the deformation monitoring points to receive satellite signals, and the observation time was required to be at least 60 min according to the grade (i.e., Grade D) in the measurement of the ground-surface deformations. The GPS receivers used were of the Topcon-HiPer IIG type, which can receive and process multiple signal types. As a result, their general survey accuracies in the horizontal and vertical directions (static survey mode) are 3 mm + 0.5 ppm and 5 mm + 0.5 ppm, respectively.

Using the data monitored in situ, the baseline solution and network adjustment were processed using the data processing software MAGNET Tools. The three-dimensional (3-D) coordinates of each monitoring point could then be obtained using the calculated baseline length and coordinates of the two fixed reference points. The displacement of a particular monitoring point at this moment in time can then be determined by calculating the difference between its current and previous coordinate values. The



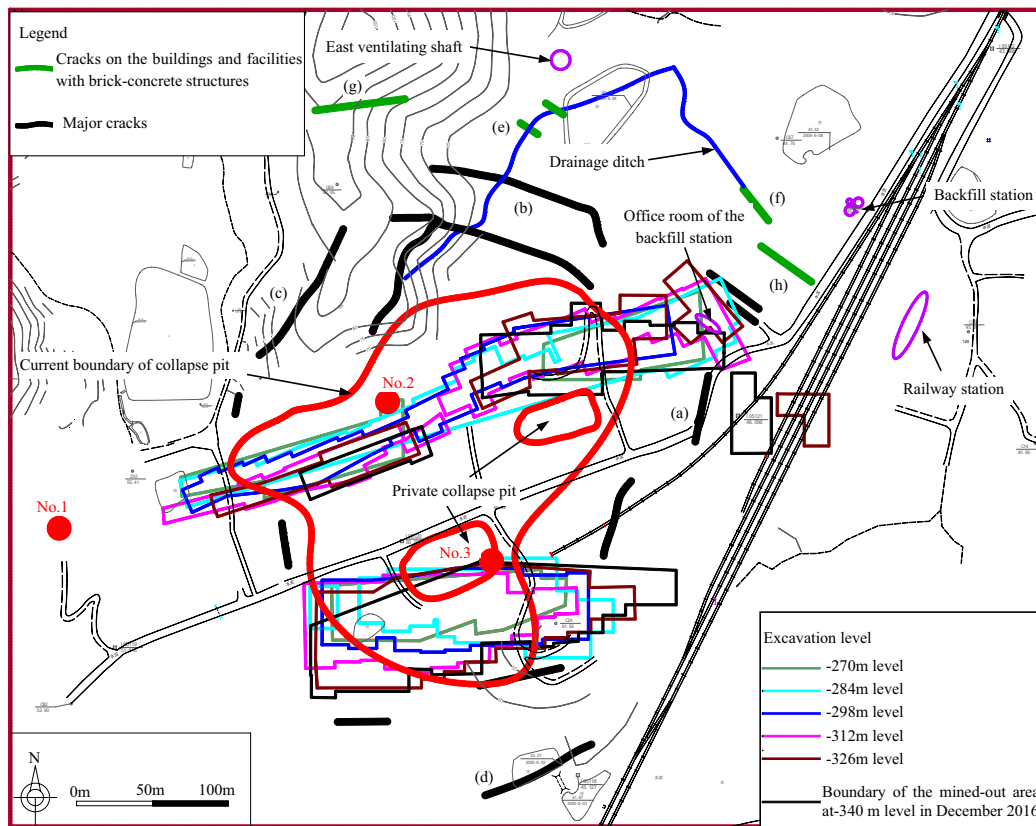


**Fig. 6** Distribution of the ground surface collapses and cracks in the mining-induced areas (the major cracks intersected with the drainage ditch, the branched major crack as well as the major crack parallel to

the branched major crack were investigated in December 2014, and other cracks were investigated in December 2016)

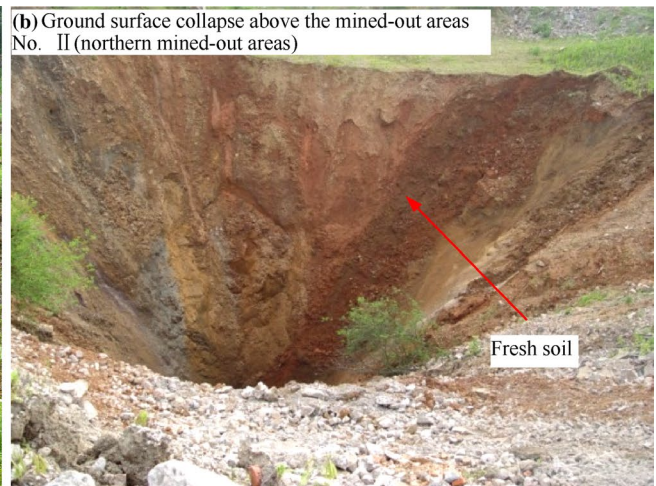


**Fig. 7** Ground surface collapses above the mined-out areas

accumulative displacement can also be determined starting from the beginning of the monitoring process. In some key areas that are influenced by mining activity, high-precision digital levels (Leica DNA03) were employed to measure

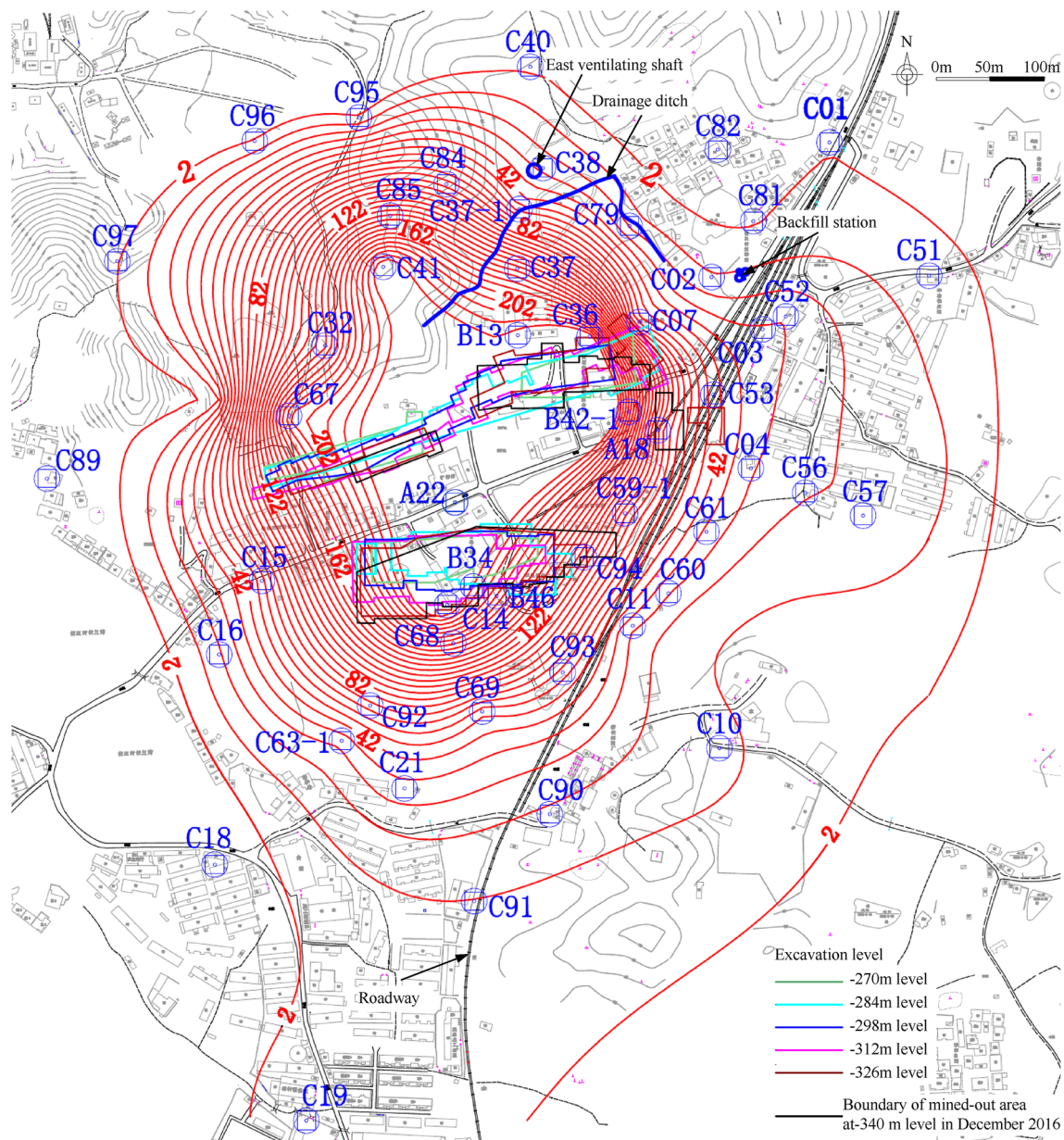
the vertical displacement of the flat ground surface. Overall, 37 level-monitoring points were employed (Fig. 9b). The measurement methods adopted were: the closed leveling method for the main line, the second-grade leveling





Fig. 8 The cracks on the ground surface, the buildings and facilities (the location of these cracks is seen in Fig. 6)





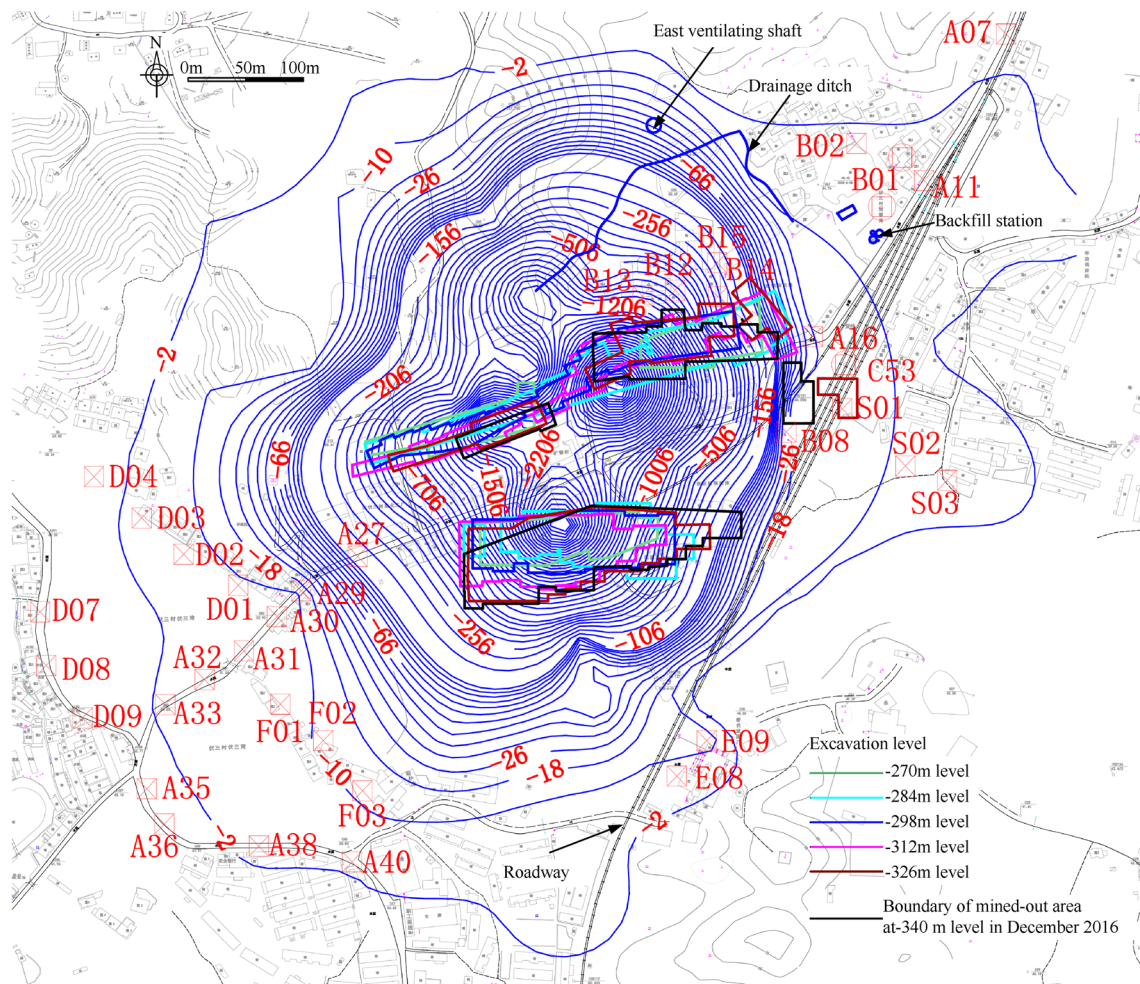
(a) Contour map of the horizontal displacements (all blue numbers refer to the GPS monitoring points, and the interval is 8 cm between two displacement contours)

**Fig. 9** Contour maps of the horizontal and vertical displacements from April 2008 to December 2016 (unit: cm)

method for the grade and the branch leveling method for the scatter of the points near the main line. Measurements were taken once a month before March 2015, and once every 2 months thereafter.

A 3-D laser-scanning system (Leica HDS 8800) was employed in December 2016 to investigate the subsidence of the ground-surface in the collapse area. This system uses a non-contact method of measurement and so it can be used to monitor locations susceptible to collapse which would otherwise be inaccessible without endangering the

safety of on-the-ground surveyors. The scanning process involves data acquisition in the field and indoor data processing. Data collection consists of three steps: (1) Select an area with good visibility, set up the tripod and place the scanner on the tribrach. This survey station is called the ‘front sight point’; (2) Insert the battery, turn on the scanner and align the telescope with the ‘back sight point’; (3) After all instruments have been correctly installed, set the scan parameters in the hand-held controller (point density, light conditions of the preview photograph, names of the



(b) Contour map of the vertical displacements (all red numbers refer to the level monitoring points, and the interval is 8 cm outside the -106cm displacement contour, and the interval is 50cm between -106cm and -506cm, and 100 cm elsewhere)

Fig. 9 (continued)

front and back sight points, scanner height, etc.). In general, the number of survey stations required is determined by the area of the collapse pit; for this mine, the number was set to 3.

The indoor data processing stage begins with the importing of the field data into the post-processing STUDIO software of the 3-D laser-scanning system. The large amount of point cloud data obtained from the scanning equipment can then be processed in various ways (matching point pairs according to the coordinates of the front and back sight points, filtering the scanning data, creating topographical models and generating contour lines, etc.). Once a topographic map of the collapsed area is obtained, it can be compared with the original topographic map from 2006. The difference between the two yields the current level of subsidence of the ground-surface in the collapse area.

The GPS and level-monitoring results obtained using the scheme outlined above are listed in Tables 8 and 9 for the eight-year monitoring period employed. The ratios of the horizontal to vertical displacements (HD/VD) at the different monitoring points can also be deduced from the data, giving the results shown in Fig. 10. Combining these results with the subsidence values derived from the laser scanning data allows contour maps to be drawn showing the horizontal and vertical displacements occurring during the period April 2008 to December 2016 (Fig. 9, which was created using the SURFER software package using the very flexible kriging method of interpolation between monitoring points). Moreover, vertical and horizontal displacement funnels can be drawn for selected profiles. For example, Fig. 11 shows displacement funnels for profile I (along exploration line 34). Finally, displacement–time curves were also derived for representative monitoring points (Figs. 12, 13, 14).

**Table 8** Monitoring results from representative GPS monitoring points

Monitoring point	Time	Cumulative deformation (unit: cm)			Direction	Time	Cumulative deformation (unit: cm)			Ratio	
		$H_N$	$H_E$	$H$			$H_N$	$H_E$	$H$		$V$
A18	Jun 2014 to Dec 2016	8.86	-38.36	39.37	Northwest	Jun 2014 to Dec 2016	8.86	-38.36	39.37	-21.73	1.81
B42-1	Oct 2012 to Dec 2016	53.69	-288.75	293.70	Northwest	Oct 2012 to Dec 2016	53.69	-288.75	293.70	-162.03	1.81
C02	Oct 2014 to Dec 2016	-1.58	-2.41	2.88	Southwest	Oct 2014 to Dec 2016	-1.58	-2.41	2.88	-0.86	3.34
C03	Apr 2008 to Dec 2016	1.48	-28.06	28.10	Northwest	May 2009 to Dec 2016	1.81	-25.54	25.60	-8.79	2.91
C04	Apr 2008 to Dec 2016	4.84	-26.77	27.21	Northwest	May 2009 to Dec 2016	4.92	-26.34	26.79	-11.44	2.34
C07	Oct 2014 to Dec 2016	-6.82	-17.45	18.74	Southwest	Oct 2014 to Dec 2016	-6.82	-17.45	18.74	-9.35	2.00
C10	Apr 2008 to Dec 2016	14.10	-3.37	14.49	Northwest	Jul 2013 to Dec 2016	9.22	-2.61	9.58	-4.34	2.21
C11	Apr 2008 to Dec 2016	28.09	-4.61	28.47	Northwest	May 2009 to Dec 2016	26.72	-3.80	26.99	-14.23	1.90
C15	Apr 2008 to Dec 2016	45.01	14.36	47.24	Northeast	May 2009 to Dec 2016	43.77	14.09	45.98	-25.35	1.81
C19	Apr 2008 to Dec 2016	6.96	1.25	7.08	Northeast	Jul 2013 to Dec 2016	6.11	0.72	6.15	-1.67	3.68
C21	Apr 2008 to Dec 2016	30.65	0.39	30.66	Northeast	May 2009 to Dec 2016	28.29	1.16	28.32	-11.26	2.51
C32	Apr 2008 to Dec 2016	-118.32	91.99	149.87	Southeast	May 2009 to Dec 2016	-115.79	91.00	147.27	-214.74	0.69
C36	Apr 2008 to Dec 2016	-153.47	-202.24	253.88	Southwest	May 2009 to Dec 2016	-150.44	-198.87	249.36	-374.16	0.67
C37-1	Aug 2015 to Dec 2016	-7.24	-1.54	7.40	Southwest	Aug 2015 to Dec 2016	-7.24	-1.54	7.40	-4.88	1.52
C38	Aug 2015 to Dec 2016	-0.86	-0.74	1.13	Southwest	Aug 2015 to Dec 2016	-0.86	-0.74	1.13	-0.29	3.87
C41	Apr 2008 to Dec 2016	-168.82	173.00	241.72	Southeast	May 2009 to Dec 2016	-166.65	173.15	240.32	-181.22	1.33
C51	Apr 2008 to Dec 2016	4.02	-4.25	5.85	Northwest	Jul 2013 to Feb 2017	4.29	-3.92	5.84	-2.87	2.03
C52	Apr 2008 to Dec 2016	5.16	-25.52	26.03	Northwest	May 2009 to Dec 2016	2.39	-24.57	24.68	-9.73	2.54
C53	Apr 2008 to Dec 2016	5.29	-45.16	45.47	Northwest	Jul 2009 to Dec 2016	2.69	-42.46	42.55	-19.29	2.21
C56	Sept 2013 to Dec 2016	7.83	-9.50	12.31	Northwest	Sept 2013 to Dec 2016	7.83	-9.50	12.31	-6.89	1.79
C57	Apr 2008 to Dec 2016	6.81	-17.03	18.34	Northwest	May 2009 to Dec 2016	6.90	-15.01	16.52	-9.88	1.93
C59-1	Oct 2014 to Dec 2016	16.58	-32.53	36.51	Northwest	Oct 2014 to Dec 2016	16.58	-32.53	36.51	-24.05	1.52
C60	Apr 2008 to Dec 2016	24.99	-7.95	26.22	Northwest	May 2009 to Dec 2016	22.57	-6.74	23.56	-14.72	1.60
C61	Apr 2008 to Dec 2016	13.74	-28.91	32.01	Northwest	Jul 2013 to Dec 2016	11.22	-20.58	23.44	-20.46	1.15
C63-1	Apr 2008 to Dec 2016	28.08	0.01	28.09	Northeast	May 2009 to Dec 2016	26.03	1.04	26.05	-18.24	1.43
C69	Jun 2014 to Dec 2016	22.15	-0.21	22.15	Northwest	Jun 2014 to Dec 2016	22.15	-0.21	22.15	-17.96	1.23
C79	Apr 2008 to Dec 2016	-13.25	-9.31	16.20	Southwest	May 2009 to Dec 2016	-10.33	-7.99	13.06	-9.73	1.34
B13	Apr 2009 to Aug 2013	-180.52	152.75	236.47	Southeast	Apr 2009 to Aug 2013	-180.52	152.75	236.47	-213.30	1.11
C37	Jun 2013 to Sep 2014	-105.03	96.56	142.67	Southeast	Jun 2013 to Sep 2014	-105.03	96.56	142.67	-198.58	0.72

$H$  and  $V$  are the cumulative horizontal and vertical displacements, respectively. The former is further decomposed into two components:  $H_N$  (north component) and  $H_E$  (east component) so that

$$H = \sqrt{H_N^2 + H_E^2}$$



**Table 9** Cumulative vertical displacements from representative level-monitoring points (unit: cm)

Monitor- ing point	Time	Vertical dis- placement	Monitor- ing point	Time	Vertical displace- ment
A05	Mar 2008 to Dec 2016	- 0.93	B01	Mar 2008 to Dec 2016	- 5.60
A06	Mar 2008 to Dec 2016	- 0.86	B02	Mar 2008 to Dec 2016	- 3.40
A07	Mar 2008 to Dec 2016	- 1.15	B08	Mar 2008 to Dec 2016	- 18.45
A11	Mar 2008 to Dec 2016	- 2.11	C53	Apr 2013 to Dec 2016	- 11.01
A18	Oct 2014 to Dec 2016	- 25.72	D01	Mar 2008 to Dec 2016	- 8.81
A29	Mar 2008 to Dec 2016	- 9.64	D02	Mar 2008 to Dec 2016	- 7.30
A30	Mar 2008 to Dec 2016	- 8.22	D03	Mar 2008 to Dec 2016	- 3.78
A31	Mar 2008 to Dec 2016	- 6.84	D04	Mar 2008 to Dec 2016	0.01
A32	Mar 2008 to Dec 2016	- 4.04	D07	Mar 2008 to Dec 2016	- 1.35
A33	Mar 2008 to Dec 2016	- 2.18	D08	Mar 2008 to Dec 2016	- 1.55
A35	Mar 2008 to Dec 2016	- 1.74	D09	Mar 2008 to Dec 2016	- 2.48
A36	Mar 2008 to Dec 2016	- 1.06	E08	Mar 2008 to Dec 2016	- 7.31
A38	Mar.2008 to Dec 2016	- 3.82	E09	Mar 2008 to Dec 2016	- 10.96
A40	Mar 2008 to Dec 2016	- 8.22	F01	Mar 2008 to Dec 2016	- 6.51
A44	Mar 2008 to Dec 2016	- 2.01	F02	Mar 2008 to Dec 2016	- 12.14
A47	Mar 2008 to Dec 2016	- 1.64	S01	Mar 2008 to Dec 2016	- 15.63
A48	Mar 2008 to Dec 2016	- 1.77			

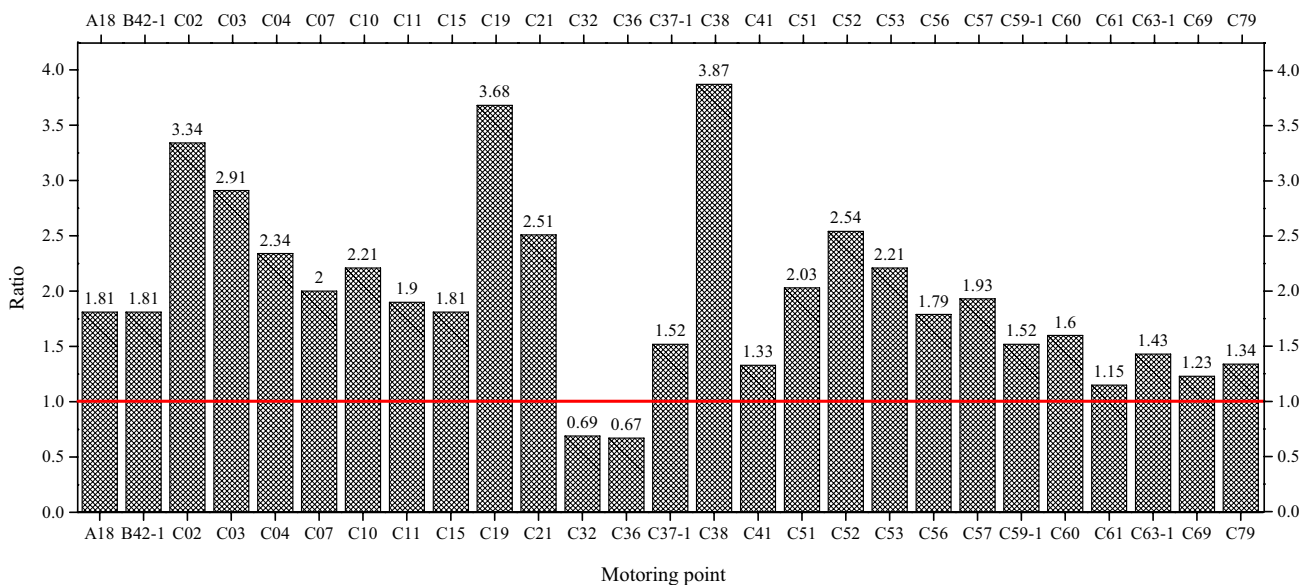


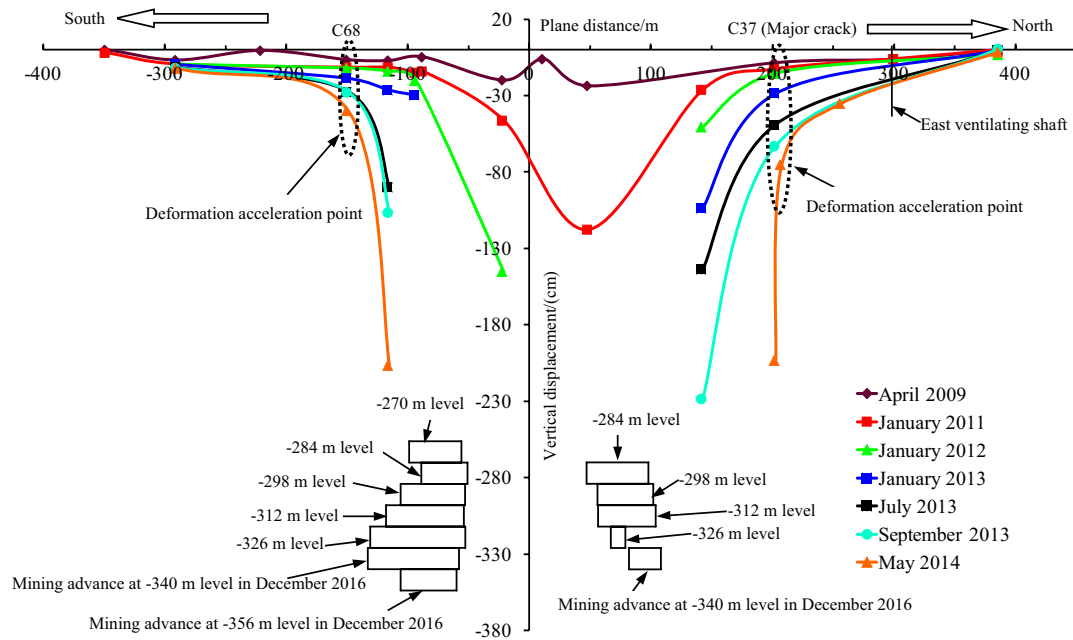
**Fig. 10** Ratio of the horizontal to vertical displacements from the monitoring points

**Characteristics of the global ground deformation**

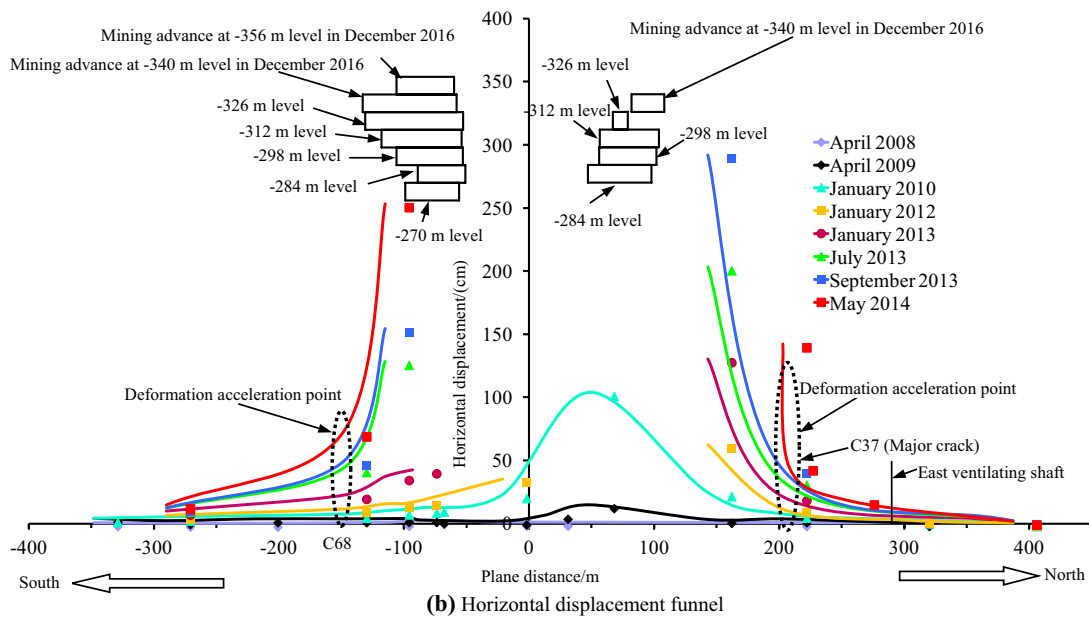
The contour maps presented in Fig. 9 show that the morphological distributions of the vertical and horizontal displacements are generally consistent with those of the mined voids. More importantly, the closer one is to the boundaries of the mined voids, the greater the displacement encountered. Clearly, the displacement decreases significantly as one moves further away from the mined voids. We also note

that the vertical displacement is generally over 10 m at the rock mass wall between the southern and northern mined voids. The main reason for this is that the F3 and F4 faults are located at the rock mass wall. Hence, the rock masses can slide relatively easily along the fault surfaces in this area under the effect of gravity.

The mining-induced displacements in the area of the foot-wall are clearly larger than those of the hanging wall. In fact, the footwall surface near the mined voids was subjected



(a) Vertical displacement funnel

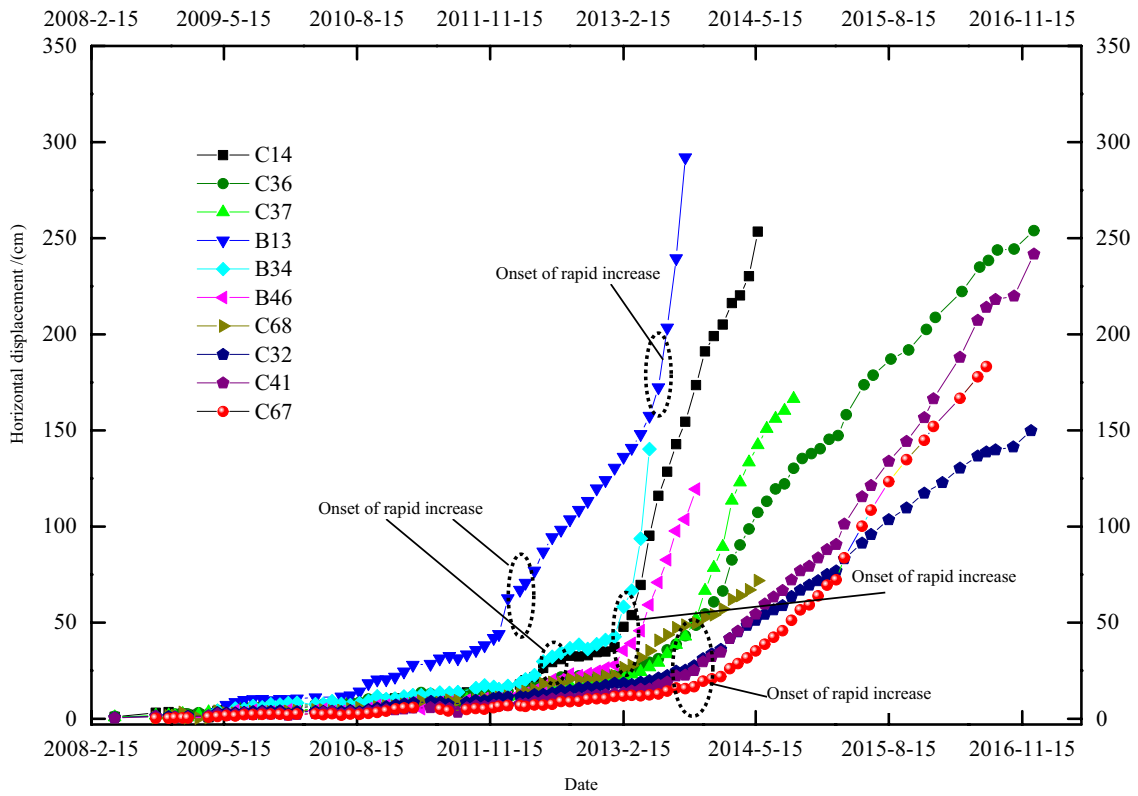


(b) Horizontal displacement funnel

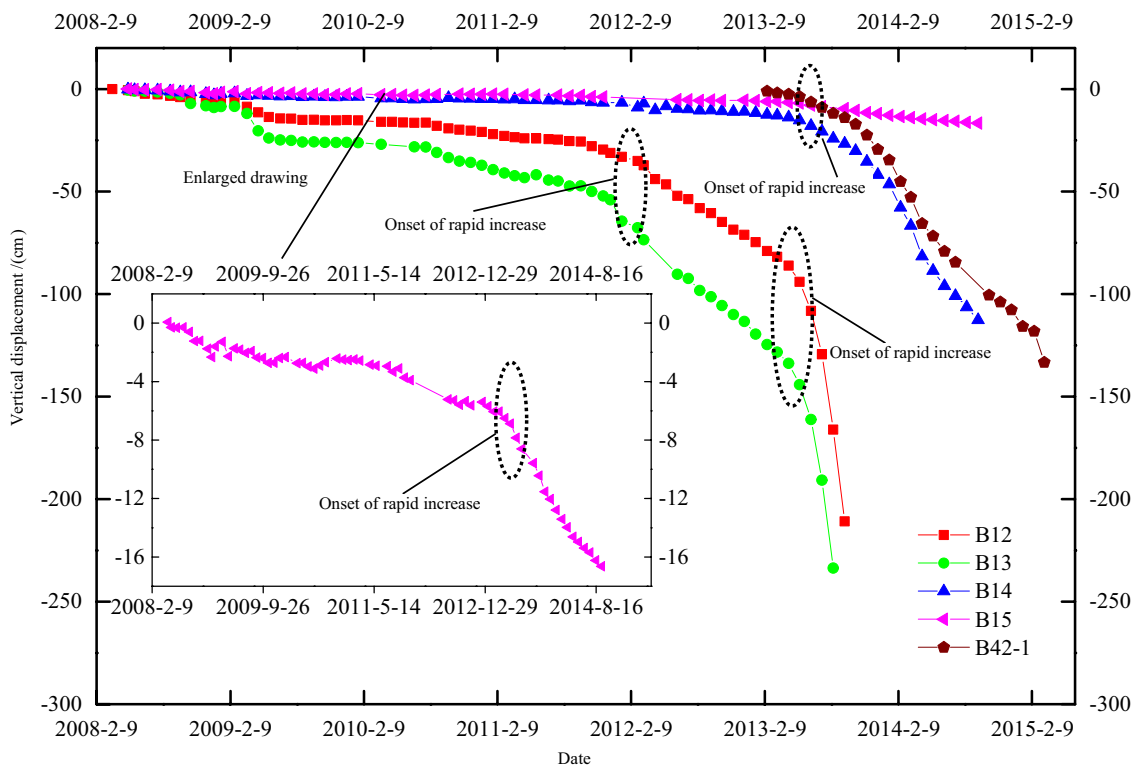
Fig. 11 Vertical and horizontal displacement funnels at profile I

to massive deformation. As an example, considering the period from June 2014 to December 2016, near the footwall, the cumulative horizontal and vertical displacements at point C41 (~ 130 m from the boundary of the mined voids) reached 1821.0 and 1381.4 mm, respectively. In contrast, the corresponding figures for the hanging wall are only 221.5 and 179.6 mm, respectively, at point C69 (~ 100 m from the boundary of the mined voids). In addition, displacements

over 5 m are widely found inside the zone encircled by the major cracks in the footwall, and currently the vertical and horizontal deformations increase with monthly displacements exceeding 50 mm (at points C36 and C41).

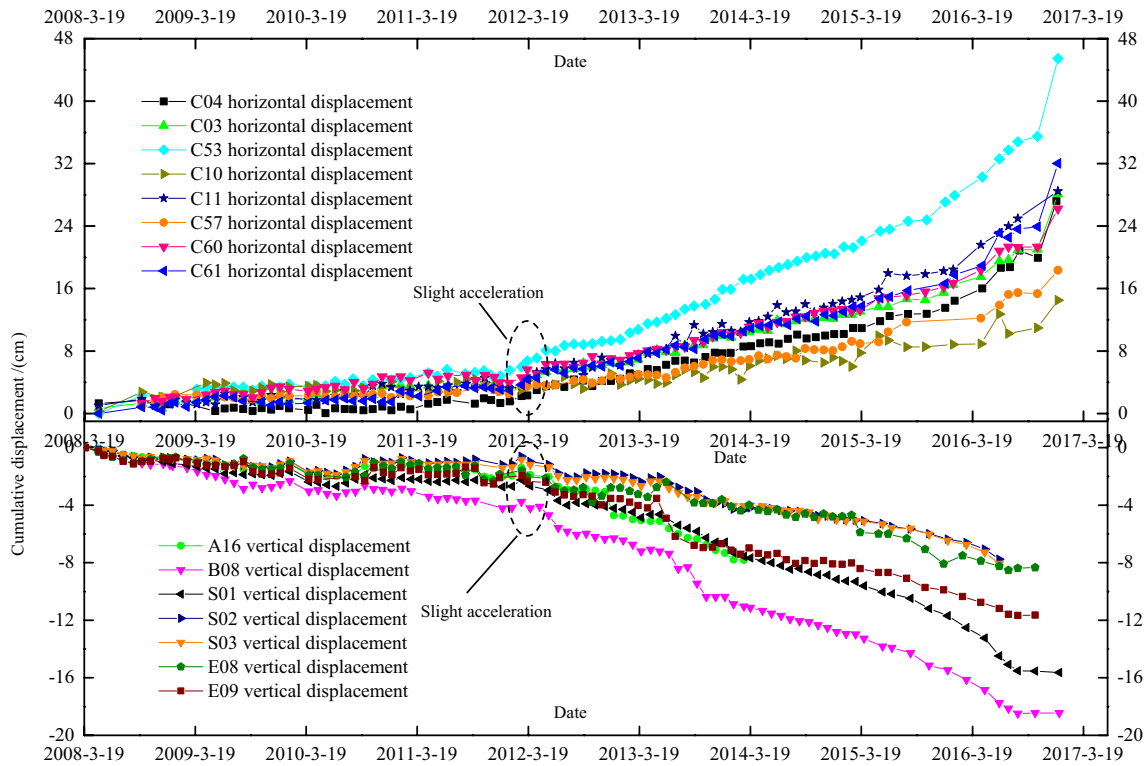


(a) Horizontal displacement

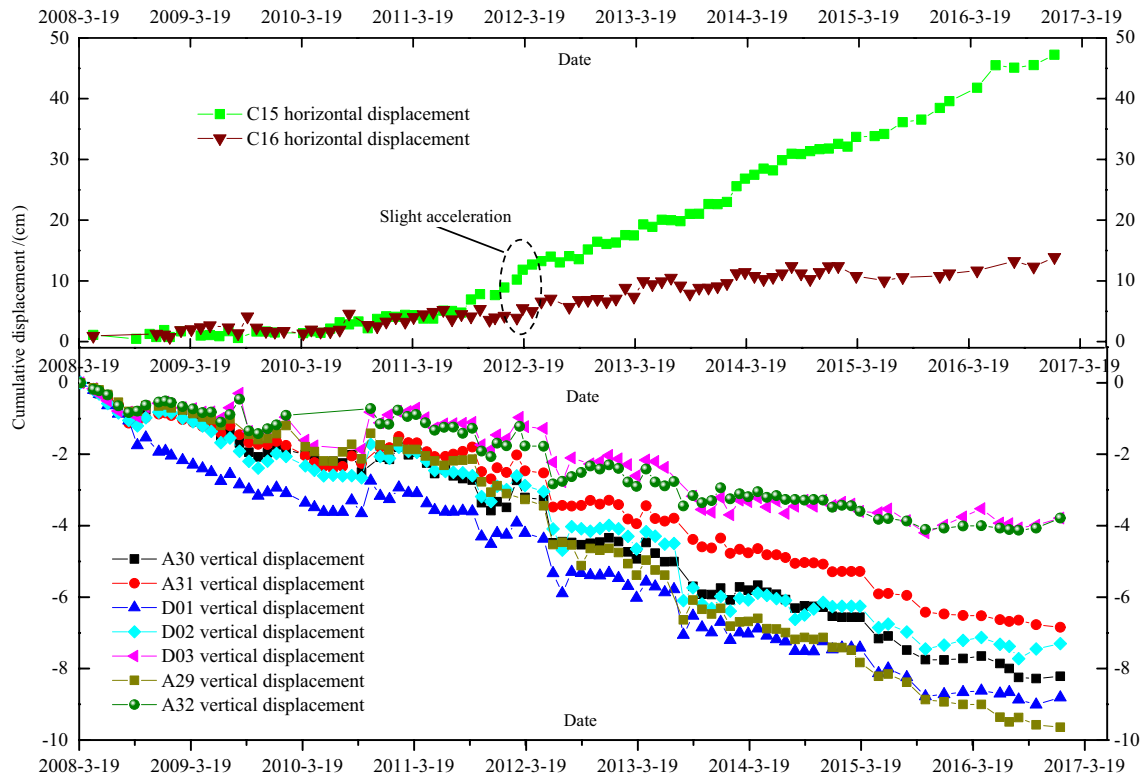


(b) Vertical displacement

Fig. 12 Displacement–time curve around the collapse pit

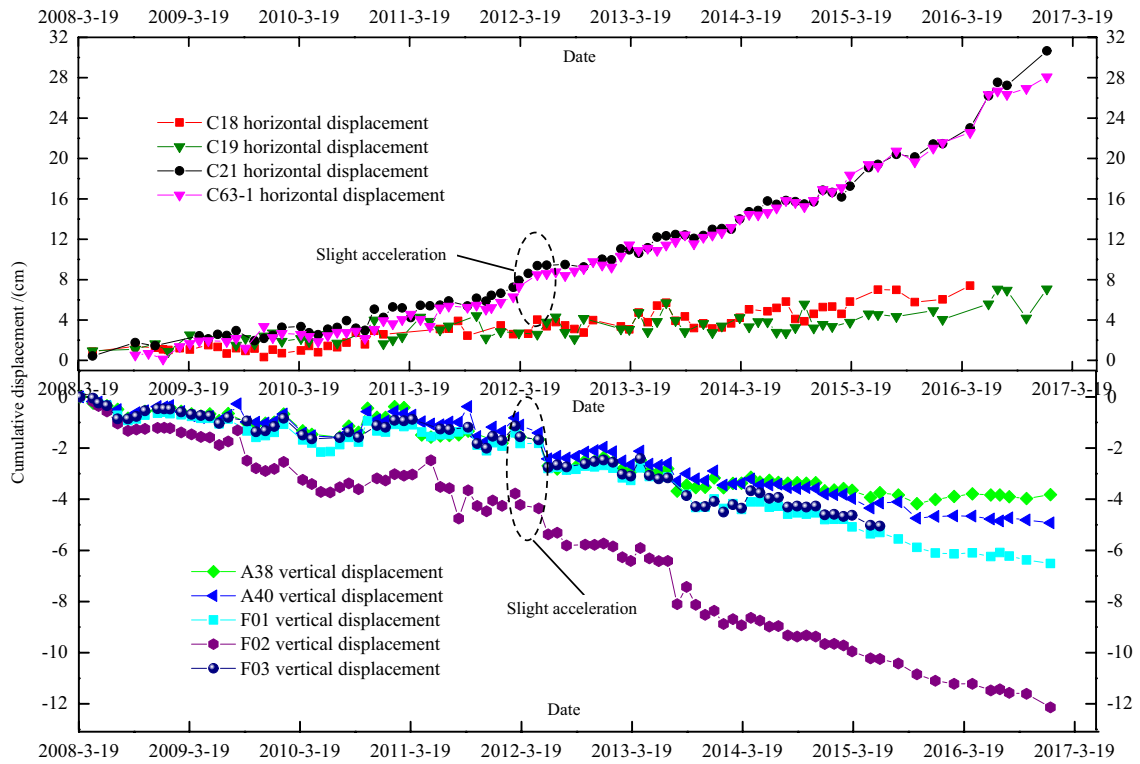


(a) Eastern part of the collapse pit

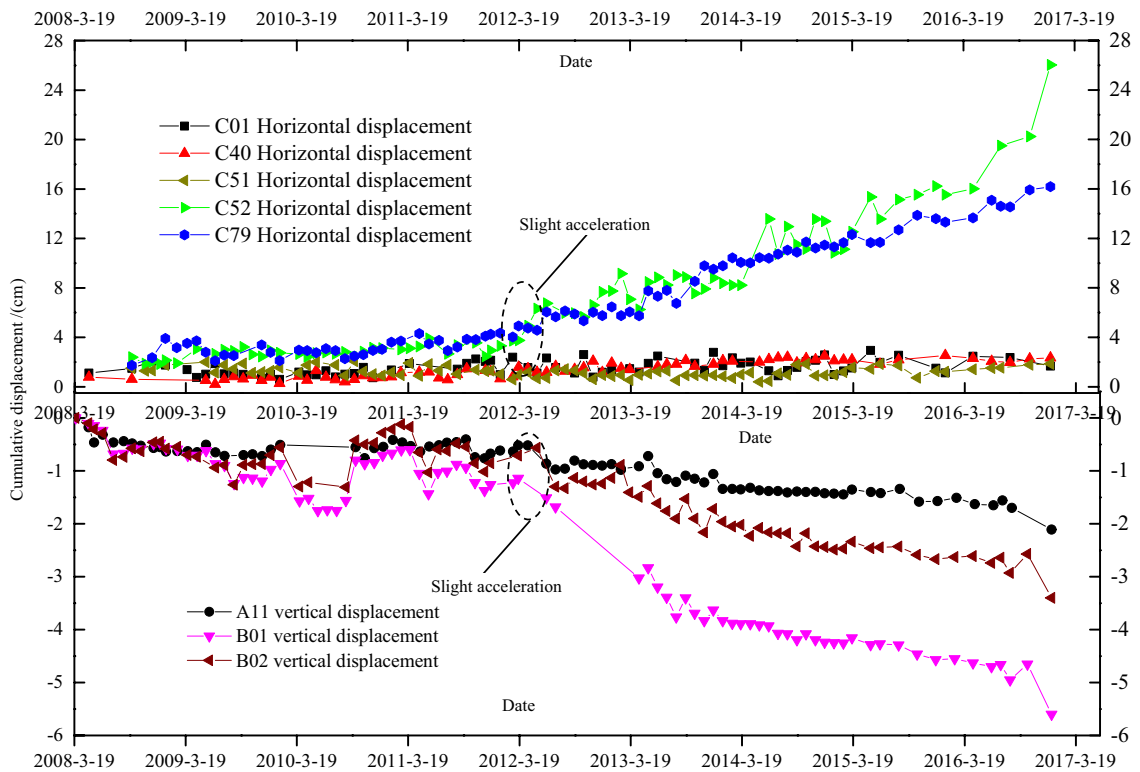


(b) Western part of the collapse pit

Fig. 13 Displacement–time curve around the eastern and western parts of the collapse pit



(a) Southern part of the collapse pit



(b) Northern part of the collapse pit

Fig. 14 Displacement–time curve around the southern and northern parts of the collapse pit



### Characteristics of the horizontal to vertical displacement ratio

As can be seen from Table 8 and Fig. 10, only a few monitoring points near the boundary of the mined voids are found to have HD/VD ratios of less than 1.00, i.e., monitoring points C32 (0.69) and C36 (0.67)). Therefore, this ratio is generally greater than 1.00 for the majority of the monitoring points (where it may reach up to 3.87). Moreover, the ratio gradually increases as the distance from the boundary of the mined voids increases. For example, in the southern part of the mining-affected area, the ratio increases in the sequence C69 (1.23) to C63-1 (1.43) to C21 (2.51) to C19 (3.68) as one moves away from the mined-out voids. This latter value is roughly three times that at C69.

### Characteristics of the vertical and horizontal displacement funnels

As shown in Fig. 11a, the subsidence funnel generally extended in a homogeneous manner in the initial stages of mining. Also, an obvious subsidence center could be discerned in January 2011 located generally in the center of the northern mined voids. At that time, the deformation of the rock mass wall between the southern and northern mined voids had become very large. For example, the cumulative vertical deformation at the monitoring point A22 reached 1449.5 mm from April 2008 to January 2012, and the vertical deformation rate in January 2012 was 1.43 mm/d. After January 2012, in the northern mining area (i.e., north of the origin point O in the coordinate axis  $x$ , see Fig. 11a), a deformation acceleration point was found at the location corresponding to the monitoring point C37 (major crack in the ground surface). The vertical displacement was small in the northern part of the monitoring point C37. However, the vertical displacement rapidly accelerated in the southern part of the monitoring point C37. For example, the rate of change of the vertical displacement at the monitoring point C37 changed from 0.13 mm/d (in December 2011) to 6.84 mm/d (in November 2013).

Similarly, in the southern mining area (i.e., south of the origin point O in the coordinate axis  $x$ , see Fig. 11a), a deformation acceleration point was found at monitoring point C68, and the vertical displacement was small in the southern part of the monitoring point C68. However, the vertical displacement rapidly accelerated in the northern part of monitoring point C68. For example, the rate of vertical displacement at monitoring point C14 changed from 0.28 mm/d (in December 2011) to 2.64 mm/d (in November 2013).

Comparing the relationship between the position of the deformation acceleration point and distribution of the mined-out areas, the deformation acceleration point in the northern mining area can be seen to be 100 m away from

the boundary of the mined-out area there. At the deformation acceleration point, the vertical displacement reached 203.09 cm from April 2008 to May 2014. However, the deformation acceleration point in the southern mining area was 15 m away from the boundary of the mined-out areas, and the vertical displacement at this point reached 39.7 cm over the same period. Hence, the deformation in the mining-affected area of the footwall was clearly larger than that of the hanging wall, in good agreement with the results from the aforementioned analysis. Also, as can be seen from Fig. 11b, the pattern shown by the horizontal displacement funnel along profile I (exploration line 34) is the same as that shown by the vertical displacement funnel.

### Displacement–time characteristics

Figure 12 shows the horizontal and vertical displacements of the surface as a function of time. As can be seen, there are several, obvious, onset points at which the displacement rapidly increases in the area associated with the collapse. Xia et al. (2016) have reported observing several typical types of displacement–time curve at the Chengchao Iron-ore Mine in China, which they refer to as ‘folding’, ‘S’ and ‘linear’. Of these, the folding-type corresponds to the appearance of points marking the obvious onset of rapid changes in displacement. Thus, the displacement–time curves observed near the collapse pit in the Jinshandian Iron Ore Mine in this work can be seen to be of the folding-type.

However, some of the displacement–time curves in Fig. 12 show two obvious onset points. For the situation in which there is one obvious onset point, the deformation of the ground surface can be split into two distinctive stages corresponding to ‘stable deformation’ and ‘rapid deformation’. This is the kind of deformation behavior that mainly occurs in the region around the collapse pit of orebody II, e.g., the GPS points C36, C37, C32, C41 and C67, and level-monitoring points B14 and B15. The periods and characteristics of the ‘stable deformation’ and ‘rapid deformation’ stages are illustrated in Table 10. We note that the onset of the rapid increase is delayed in the second deformation stage, to some degree, at monitoring points that are slightly further out from the mined-out areas, e.g., the onset of the rapid increase at point C67 occurred in June 2013, while at points C37, C32 and C41 it happened in July 2013. Therefore, when the displacement–time curve has two obvious onset points, the ground surface appears to experience three distinctive behavioral patterns which could be referred to as ‘stable deformation’, ‘rapid deformation’ and ‘even faster deformation’. This is the kind of deformation behavior that mainly occurs in the regions around the collapse pits of both orebodies II and I, e.g., the GPS point B13 and level-monitoring points B12 and B13 around the collapse pit of

**Table 10** Ground-surface deformation characteristics in the region around the collapse pit of orebody II

Number of the onset point	Stage	Period	Deformation characteristics
One onset point	The first stage (stable deformation)	The privately-mined ground collapsed to April 2013	The deformation increased stably, i.e., the deformation rate remained nearly constant
	The second stage (rapid deformation)	May 2013 to December 2016	The deformation increased rapidly while the deformation rate again remained nearly constant (the deformation rate, however, is at least six times greater than that in the first stage)
Two onset points	The first stage (stable deformation)	The privately-mined ground collapsed until February 2012	The deformation increased stably, i.e., the deformation rate remained nearly constant
	The second stage (rapid deformation)	March 2012 to April 2013	The deformation increased rapidly while the deformation rate remained generally constant (at ~3–5 times that in the first stage)
	The third stage (even faster deformation)	May 2013 to December 2016	The deformation increased even more rapidly, with the deformation rate generally remaining constant at ~5–7 times that in the second stage

**Table 11** Ground-surface deformation characteristics in the region around the collapse pit of orebody I

Number of the onset point	Stage	Period	Deformation characteristics
Two onset points	The first stage(stable deformation)	The privately-mined ground collapsed to February 2012	The deformation increased stably with a constant deformation rate
	The second stage (rapid deformation)	March 2012 to January 2013	The deformation increased rapidly and the deformation rate remained generally constant (at ~3–6 times that in first stage)
	The third stage (even faster deformation)	February 2013 to December 2016	The deformation increased even more rapidly, and the deformation rate remained generally unchanged (at about 3–11 times that in the second stage)

orebody II, and the GPS points C14, B34, B46, and C68 around the collapse pit of orebody I (see Tables 10 and 11).

As seen in Figs. 13 and 14, the ground deformations for most of the representative monitoring points in the northern-, southern-, western- and eastern-parts of the mining-affected areas began to slightly accelerate from March 2012 (the deformation was up to six times higher than that before March 2012). For example, the horizontal displacement of point C15 (~70 m from the western boundary of the southern mined-out area) increased monthly by approximately 2.10 mm before March 2012 and about 6.47 mm after March 2012. After that, the deformation at these monitoring points increased steadily.

Hence, based on the aforementioned time-dependent deformation characteristics, the ground deformation in the mining-affected area had two obvious onset times at which it underwent rapid increases: the first occurred in March 2012. For the rock masses around the collapse pit of orebody I, the

second time occurred in February 2013. However, for the rock masses around the collapse pit of orebody II, the second time occurred in May 2013. Combined with the mining conditions, the reason why the ground deformation rapidly increased in March 2012 is that the mining activity restarted then. The macroscopic signs of failure seen on the ground surface also suggest the reason for the second rapid increase in deformation. That is, this behavior occurs because the rock masses are subjected to extensive unloading at the moment the ground surface collapses. This directly results in the release of a large amount of the in situ horizontal stress within the rock mass which subsequently triggers the deformation response from the rock mass.

## Investigation of the ground movement

The concepts of ‘movement angle’ or ‘break angle’ are generally employed to describe the extent of the ground surface disturbance in traditional mining engineering design. These are defined as the angles between the horizontal and an imaginary straight line drawn along either the surface movement line or break line to the active mining level (Brady and Brown 2006; Villegas et al. 2011). According to Sect. 4.3, the horizontal displacement is usually larger than the vertical displacement in the rock masses surrounding the mined voids. Therefore, the critical deformation values used to define the surface movement and break lines are usually characterized by the horizontal displacement (Cheng et al. 2014; Song et al. 2018; Deng et al. 2019). They correspond, in fact, to horizontal strains ( $\epsilon$ ) of 2 and 6 mm/m, respectively, for areas with brick/concrete buildings and facilities. Using these values, the movement and break lines in the mining-affected areas can be plotted (Fig. 15) according to the ground-surface data monitored in situ (including all 55 GPS monitoring points). The variation of the break and movement angles occurring along the typical profile I (exploration line 34) from April 2007 to December 2016 can also be constructed (Fig. 16).

### Extension characteristics of the movement and break lines

Some regular patterns can be found in the mining-induced ground movement alluded to in Fig. 15, as follows:

- (1) The break line extends 160 m beyond the boundary of the mined-out areas in the north (to I–1 in the profile) and 83 m in the south (to I–2 in the profile). Therefore, the extension of the break line in the hanging wall is significantly smaller than that in the footwall. However, the break line extends 64 m to the west (to profile II), and 63 m to the east (to profile III). By June 2014, the break line had begun to reach the railway. In September 2013, the break line reached the office room of the backfill station. Thereafter, the walls of the office room began to be subjected to large-scale cracking and it had to be relocated in December 2013. Currently, the break line lies approximately 60 m west of the backfill station, and 26 m away from the south side of the east ventilating shaft. In addition, part of the railway (approximately 270 m) is located within the break zone.
- (2) The movement line extends 213 m beyond the boundary of the mined-out areas to the north (at profile I–1), and 165 m to the south (at profile I–2). So, the extension of the movement line in the hanging wall is significantly smaller than that in the footwall, and therefore

matches the evidence from the break line. However, the movement line extends 126 m to the west (at profile II), and 120 m to the east (at profile III). By January 2013, the movement line began to reach the railway. By June 2014, the movement line had reached the halfway point in the subsidiary building of the backfill station. In September 2013, the movement line generally reached the location of the east ventilating shaft. Currently, the movement line has reached the railway station, and lies approximately 9 m from the west side of the backfill station, and part of the railway (approximately 460 m) is located within the movement zone. Hence, currently, the foundations of many buildings and facilities such as the east ventilating shaft and the railway are within the movement or even break areas.

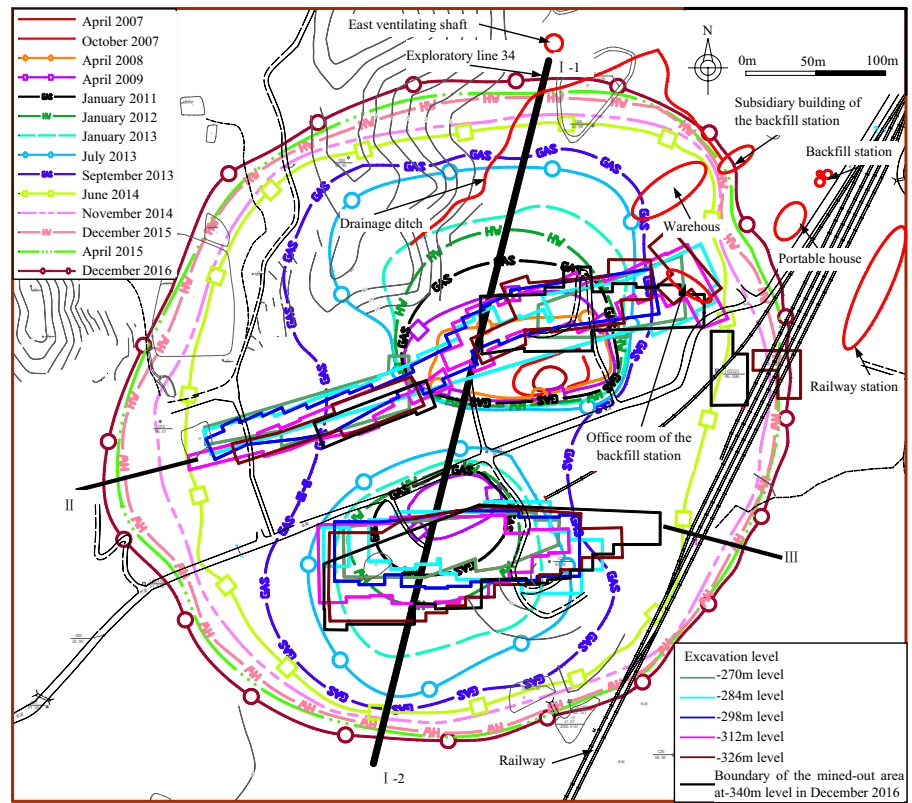
### Characteristics of the change in movement and break angles

As seen in Fig. 16, some regular patterns in the movement and break angles can be summarized as follows:

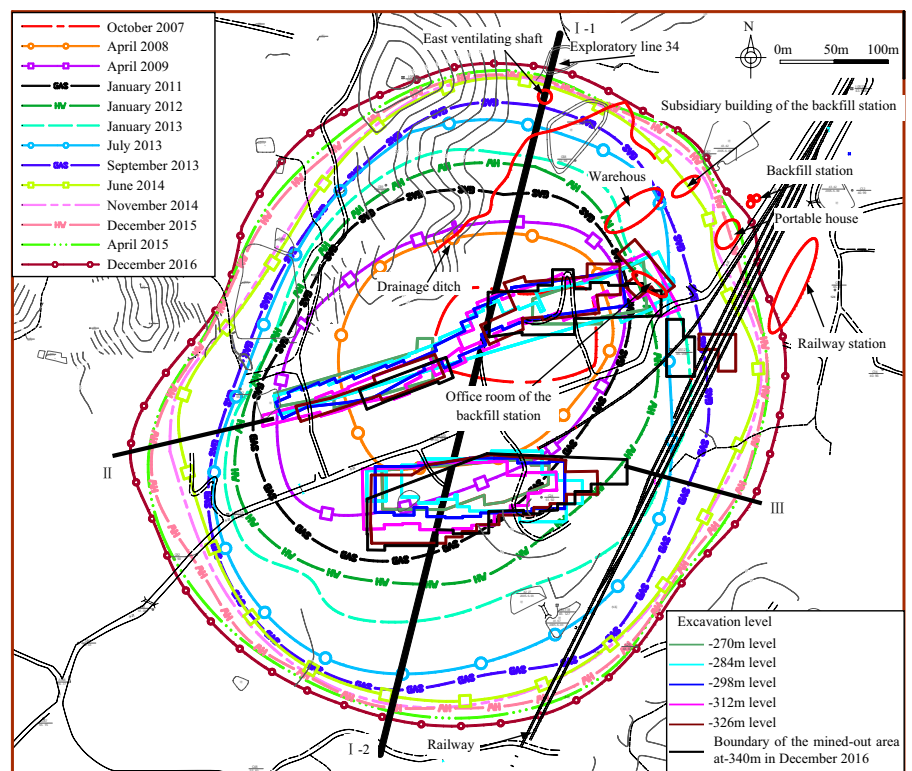
- (1) As shown by the distributions of the break angle in Fig. 16a, the break angle of the footwall generally decreased to about  $64^\circ$  in December 2016. However, the lowest break angle of the hanging wall was approximately  $75^\circ$ , occurred in June 2014, and it was larger (by approximately  $11^\circ$ ) than that of the footwall. Furthermore, the break angle decreased significantly from January 2013 to July 2013. More specifically, it decreased from  $78^\circ$  to  $73^\circ$  (i.e.,  $\sim 5^\circ$ ) in the footwall and from  $77^\circ$  to  $73^\circ$  (i.e.,  $\sim 4^\circ$ ) in the hanging wall.
- (2) As shown by the distributions of the movement angle in Fig. 16b, the movement angle of the footwall generally decreased to about  $57^\circ$  in December 2016. However, the lowest movement angle of the hanging wall was approximately  $63^\circ$ , which occurred in June 2013, and it was larger (by  $\sim 6^\circ$ ) than that of the footwall. Furthermore, the movement angle decreased significantly from January 2013 to July 2013. Actually, it decreased from  $68^\circ$  to  $64^\circ$  (by  $\sim 4^\circ$ ) in the footwall and from  $70^\circ$  to  $63^\circ$  (by  $\sim 7^\circ$ ) in the hanging wall.

Hence, the break and movement angles significantly decreased from January 2013 to July 2013 in the mine. The reason for this is that the deformation of the ground surface rapidly increased in that period after the ground surface collapsed leading to a rapid outwards extension of the ground. Moreover, the smallest break and movement angles in the Jinshandian Iron Mine all occurred in the footwall. That is, the break and movement angles in the hanging wall are larger than those in the footwall. However, the break and

**Fig. 15** Distributions of the break and movement lines: April 2007 to December 2016

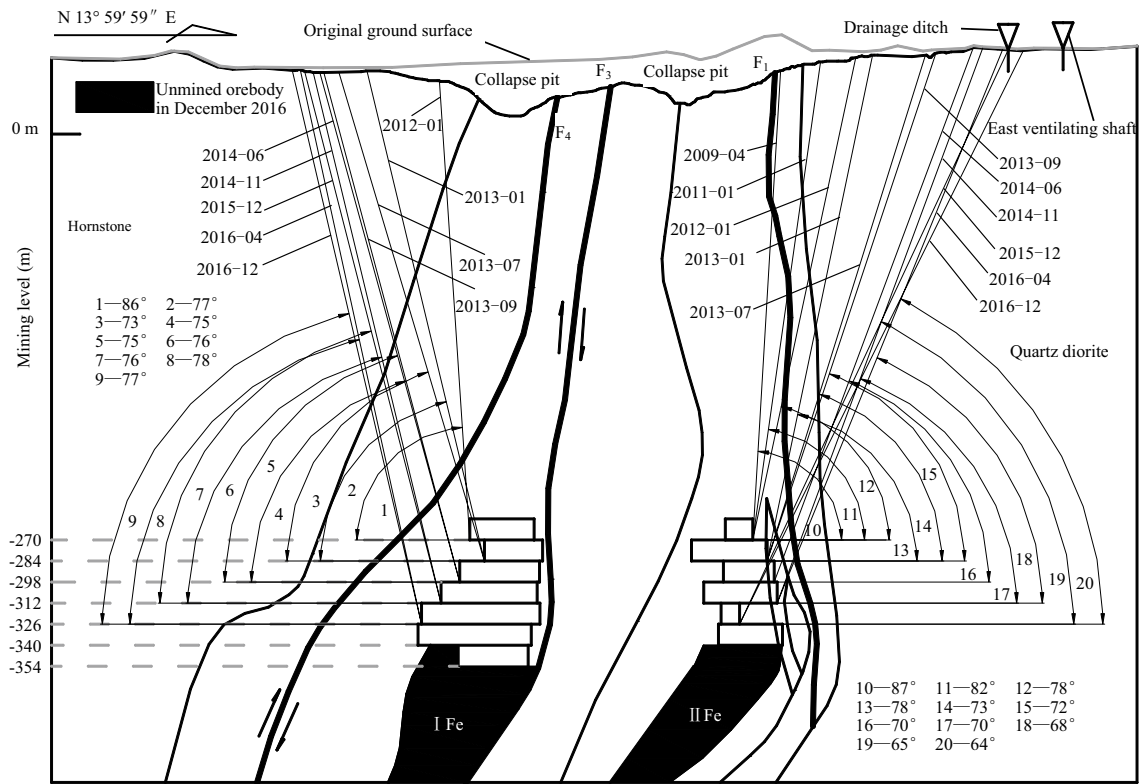


**(a)** Break line

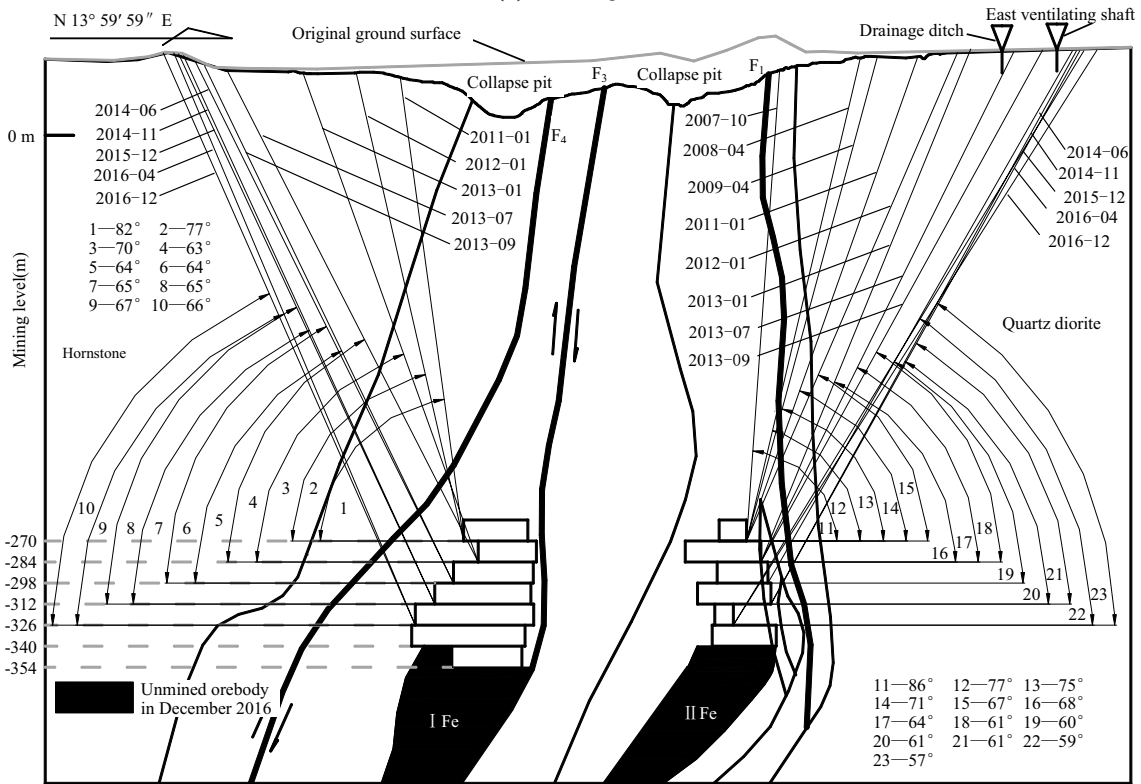


**(b)** Movement line





(a) Break angle



(b) Movement angle

Fig. 16 Distributions of break and movement angles: April 2007 to December 2016



movement angles of the hanging wall are generally smaller than those of the footwall in metal mines being mined using the SLC method without sill pillars, as found in the Kiirunavaara and Grängesberg Iron Mines in Sweden (Singh et al. 1993; John and Lupo 1997; Brady and Brown 2006; Villegas et al. 2011; Edelbro et al. 2012; Villegas et al. 2013) and the Jinchuan Nickel Mine in China (Zhao et al. 2013; Ding et al. 2018). Therefore, the patterns noted above for the ground movement in the Jinshandian Iron Mine (as observed via in situ monitoring) are the opposite of those generally found in metal mines. In other words, there is a big difference between the behaviors of the ground observed in the currently analyzed mine and that found in other metal mines.

### Mechanism responsible for the mechanical extension of the ground in the footwall

#### Movement and break angles defined in the initial mining stage

The original movement and break angles designed in the initial mining stages for the mining of the eastern part of the Jinshandian Iron-ore Mine were estimated from those found for the western part. This approach to estimating movement and break angles can be viewed as a method of analogy, i.e., the angles in the prospective mine are estimated from other mines with similar (or analogous) geological and mining conditions. Thus, based on the movement and break angles in the western mining area, the movement and break angles originally designed for the eastern mining area when the underground orebodies in the – 270 and – 340 m levels were being mined out are those illustrated in Table 12. Clearly, the break and movement angles designed in the footwall in the initial mining stage were significantly larger than those in the hanging wall (the difference amounts to 12°).

According to these originally defined angles, the locations of the key facilities and buildings of the mine (east ventilating shaft, drainage ditch, mountain road, etc.) were all arranged so as to lie outside the scope of the danger zone suggested by the angles, thus making them ‘safe’. However, the foregoing analysis of the in situ measurement data indicates that the scope of the ground movement in the footwall was significantly larger than that designed using the analogy approach. More specifically,

when mining the – 340 m level, the originally-designed movement angle in the footwall was 70°, but that obtained from the in situ data analysis was 57°, showing a difference of ~ 13°. Consequently, the foundations of many of the buildings and facilities in the footwall were prematurely engulfed within the movement-prone or even break-prone areas. Thus, these buildings and facilities were subjected to large-scale deformation and cracking much earlier than expected (Fig. 8b, e), so that the workers were forced to abandon them and relocate elsewhere.

Overall, one can thus speculate that a unique mechanism seems to be responsible for the mechanical extension of the ground of the footwall in the eastern mining area of the Jinshandian Iron Mine.

### Mechanical-extension mechanism responsible for the ground movement

From Figs. 1 and 2, it is clear that the overburden strata above orebody II are mainly comprised of marble, and that the discontinuity within the marble is quite developed. At the same time, karst cavities can be found in some local areas within the marble. Overall, the rock-mass quality of the marble falls in the poor range according to the RQD classification scheme. As the SLC method was adopted without sill pillars in the Jinshandian Iron Mine, the overburden strata were inevitably subjected to caving when the underground orebodies were extracted, and this would lead to the free displacement of the overburden strata. Due to the poor quality of the marble and presence of large-scale privately-mined voids in the overburden strata, the caving of the overburden strata would develop progressively towards the ground surface as the underground orebodies were excavated deeper and deeper.

Considering their dispositions, the fault (F<sub>1</sub>) and bedding surface between the quartz diorite—hornstone (or marble) can be regarded as left and right boundaries due to their lower resistance to movement (see Fig. 17). That is, the caving process is controlled by this bedding surface and this fault as these behave as surfaces of low shear strength. Thus, the overburden strata may slide along these surfaces under the influence of gravity. The rock mass region produced by the caved overburden strata can be considered to be the caved zone. Hence, the propagation of the caved zone to the ground surface is closely related to the geological structure within the rock mass. More precisely, it is the sliding motion along the

**Table 12** Originally designed movement and break angles of the eastern mining area when the underground orebodies in the – 270 m and – 340 m levels were mined out

Mining level (m)	Movement angle (°)			Break angle (°)		
	Hanging wall	Footwall	End part	Hanging wall	Footwall	End part
– 270 m level	58°	70°	70°	63°	75°	80°
– 340 m level	59°	70°	70°	64°	75°	80°

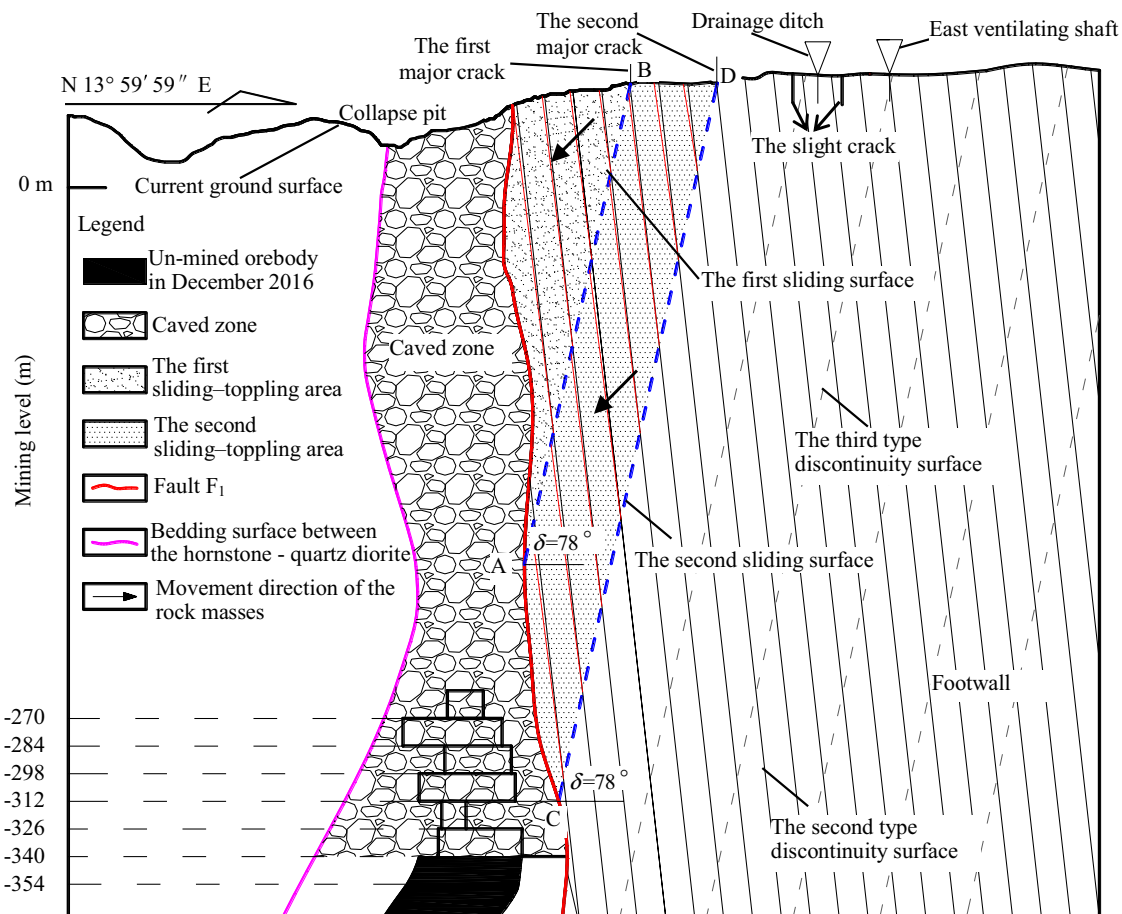


**Fig. 17** Ground movement of the rock masses surrounding the mined-out areas in the footwall ( $\delta$  refers to the dip angle of the sliding surface)

bedding, discontinuity and fault surfaces that are responsible for the instability that produces cavity propagation.

According to Sect. 2.2, there are many groups of major discontinuities found within the footwall that have very high dipping angles (mostly in the range 65–85°). The surrounding rock mass is subsequently ‘carved’ by these discontinuities into separate ‘column-shaped’ rock masses, which appear throughout the footwall. When disturbed by the excavation of underground orebodies, the rock masses surrounding the mined-out areas will undergo deformation and movement that is highly dependent on these discontinuity surfaces (which behave as paths of low resistance). Hence, the surrounding rock masses will be fractured along the discontinuity surfaces. In response to this, cracks will form in the surface of the ground in locations corresponding to the discontinuity surfaces, as manifested by the macro-failure phenomena observed at the surface (Fig. 18). In particular, the strikes of the second- and third-type discontinuities (i.e., the major discontinuities with orientations of  $20^\circ < 84^\circ$  or  $200^\circ < 83^\circ$  in Table 3) are generally consistent with those of the two major cracks intersecting the drainage ditch which have strikes of approximately

N 70° W (see Fig. 18). The strike of the fourth-type discontinuity (orientation  $287^\circ < 76^\circ$ ) is generally consistent with those of the other two major cracks which have strikes of approximately N 30° E.

Considering the distribution of the underground orebodies and key ground surface facilities and buildings, we selected the profile formed by exploration line 34 to further investigate the ground movement induced by underground mining—see Fig. 17. In this figure, the two sets of intersecting lines represent the second and third types of discontinuity (see Table 3) which dip in opposite directions (the second type of discontinuity corresponds to an anti-inclined structure). When the extent of the overburden caving reaches ground level, the ground surface will collapse and the rock masses in the collapsed area will become discrete bodies. At that moment, the rock masses surrounding the mined-out area will start to become unloaded. Based on common experience, the surrounding rock masses are expected to slide along the third-type of discontinuity surface (which behave as low shear strength surfaces) under the influence of gravity. In this case, the HD/VD ratio should range from

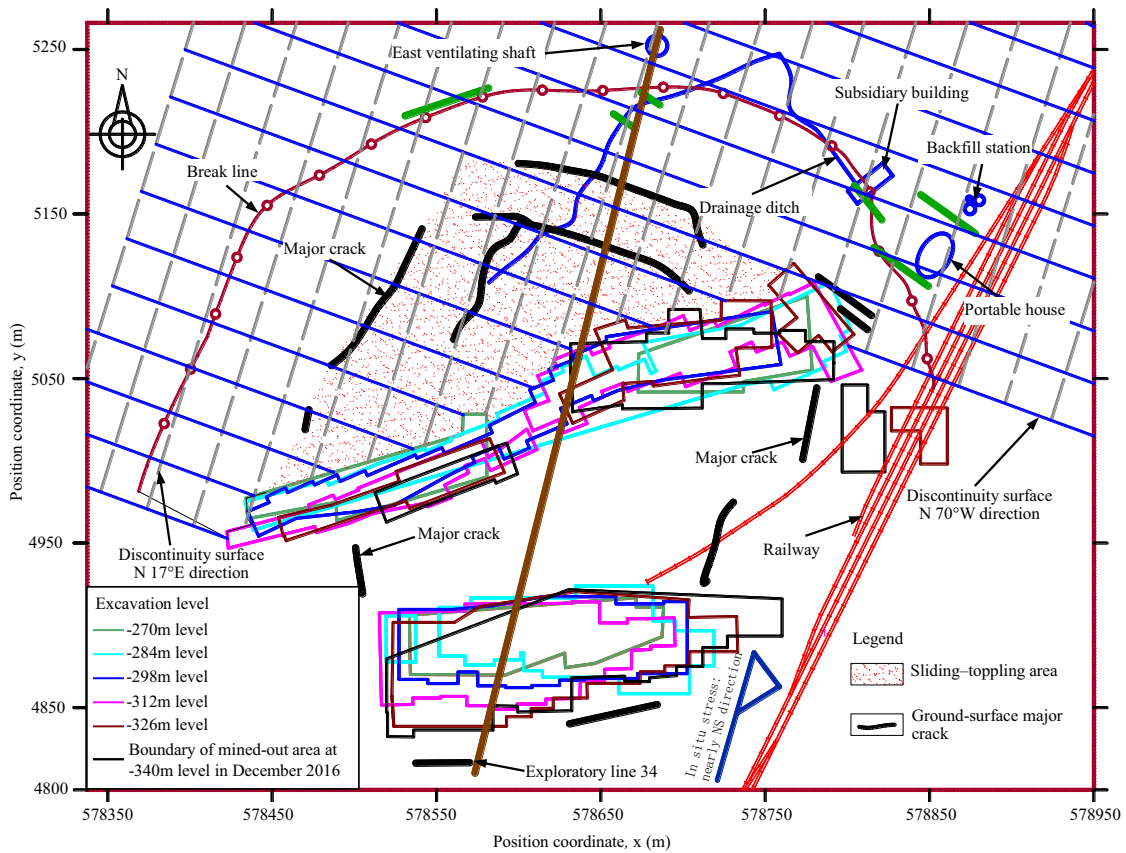


**Fig. 18** Distributions of the mined-out areas, discontinuity surfaces and ground surface cracks in the mining-induced area (the blue line represents the strikes of the second- and third-type discontinuity sur-

faces, and the grey line represents the strike of the fourth-type discontinuity surface)

0.05 to 0.29 as the dip angle ranges from 74° to 87° for the third-type discontinuity. However, the in situ deformation data suggest that the HD/VD ratios in this area are significantly larger than those calculated using the dip angles of these discontinuities (i.e., 0.05–0.29). In fact, the ratios at the monitoring points C36, C37 and B13, which are near the major crack, are 0.67, 0.72 and 1.11, respectively. Hence, another failure mechanism must also exist in the analyzed area, and so the failure mechanism acting in the rock masses surrounding the mined-out areas must be a composite one.

The collapse of the ground surface leads to a decrease in the in situ horizontal stress acting on the column-shaped rock masses near the collapse area. However, the horizontal tectonic stress acting on the other side of the column-shaped rock masses will generally remain unchanged. Thus, the horizontal forces acting on the sides of the column-shaped rock masses will become unbalanced. Consequently, the column-shaped rock masses will tend to rotate on the third-type discontinuity surfaces, that is, they are subjected to toppling. Hence, the rock masses surrounding the mined-out areas also undergo topping failure during the sliding process. This

kind of failure mode is referred to as ‘sliding–toppling’ in this study.

Clearly, the major cracks can be thought of as defining the locations of the sliding surfaces of the column-shaped rock masses (or overlapping column-shaped rock masses) at the ground-surface. The field investigations revealed that two major ground-surface cracks are to be found near exploration line 34. Therefore, there must be two obvious sliding surfaces in the rock masses surrounding the mined-out areas in this area (referred to as the first and second sliding surfaces, as the distance from the mined-out areas increases—see Fig. 17).

According to Xia et al. (2016), the time at which the displacement starts to rapidly increase (which can be determined using appropriate displacement–time curves) can be used to determine the time at which a sliding surface forms in the column-shaped rock masses. Considering the onset times observed at monitoring points B13 and C37 (Sect. 4.5), the first and second sliding surfaces in the column-shaped rock masses of the footwall in this mine can be generally considered to have formed in May 2013 and July 2013, respectively. After the sliding surfaces formed, the

column-shaped rock masses began to slide and topple along them towards the mined-out areas. We refer to these areas as ‘sliding–toppling’ areas. At the present time, slippage and tensile phenomena can be readily observed at ground level near the major cracks (Fig. 8b, c).

### Large-scale ground movement

There is likely to be a rapid change in the in situ stress field within the rock masses surrounding the mined-out area after the ground surface collapses. After it collapses, the first column-shaped rock mass layer (i.e., the first sliding–toppling area shown in Fig. 17) is subjected to forces that are not balanced, which leads to the sliding surface forming along the discontinuity surface (line AB in Fig. 17). After that, the second column-shaped rock mass layer (i.e., the second sliding–toppling area in Fig. 17) is gradually subjected to unloading effects as the mining activity extends deeper and deeper. This again causes the release of in situ stress in the column-shaped rock masses. Thus, the second sliding surface is formed along the discontinuity surface (line CD in Fig. 17). As mining continues, further sliding surfaces will form along the discontinuities producing a third, fourth, fifth, ... sliding–toppling area at distances that are progressively further away from the mined-out areas. That is, the mining-induced ground movement gradually extends outwards.

This explains why the footwall rock masses are subjected to large-scale ground movement earlier than expected. According to site investigations, only small cracks are currently found at distances of 40 m or so from the boundary of the second column-shaped rock mass layer (Figs. 6 and 8e). Hence, sliding surfaces have not yet formed along the discontinuity surfaces to produce a third (and fourth, etc.) sliding–toppling area. However, it can be speculated that such sliding surfaces will be formed in the rock mass as mining proceeds. It is likely, therefore, that the area around the east ventilating shaft will ultimately suffer deleterious effects due to these sliding surfaces and will subsequently have to be abandoned and any buildings in the area relocated.

According to the foregoing analysis, the excavation of the underground orebodies is clearly a vital factor influencing the movement of the ground in the footwall of the mine. Discontinuities within the surrounding rock mass can also significantly affect the behavior as they are geological defects. If there is a major discontinuity in the surrounding rock mass that has a strike that is generally parallel to the boundary of the mined voids, then rupture will preferentially occur along this major discontinuity. Therefore, the macroscopic deformation of the ground surface is such that the major dislocations and opening cracks are formed along the major discontinuities (see Fig. 8b, c). Hence, the presence

of discontinuities within the surrounding rock masses determines the large-scale ground movement that occurs in the footwall of the mine; they also determine the failure mode of the rock masses.

More importantly, the horizontal tectonic stress within the surrounding rock masses is the dominant tractive force that drives the ground movement to extend outwards rapidly, and it exerts a prominent effect on the ground movement. Under the action of horizontal tectonic stress (especially when the direction of the major horizontal stress is perpendicular to the strike of the discontinuity), the scope of the mining-induced ground movement will significantly exceed that anticipated in the design stage if the analogy method is used. This, for example, is what has occurred in the area to the east of the ventilating shaft in this mine, and was also quite obvious in the Chengchao underground Iron Mine (Xia et al. 2017).

### Discussion

In a mining area, the ground undergoes different deformations and movement during different stages of the mining process. Currently, the scope of the deformation and movement of the ground in the footwall is significantly larger than that in the hanging wall in the mine studied (the Jinshandian Iron Mine). However, as the underground orebodies are excavated to greater depth, the characteristics of the inclinations of the footwall and hanging wall will become more apparent. Thus, it is possible that the scope of the deformation and movement of the ground in the footwall in the mining area becomes smaller than that in the hanging wall in the future.

According to the analysis in Sect. 2.4, the current extent to which the underground orebodies have been excavated is not large (mainly ranging from the – 256 m level to the – 340 m level, a total thickness of 84 m). In addition, the dip angle of the mined-out area created by orebody excavation is very small. Thus, the inclination characteristics of the footwall and hanging wall are not obvious at the moment. Therefore, gravity is not currently having a very obvious effect on the rock mass of the hanging wall. Under such circumstances, the scope of the deformation and movement of the rock masses in the footwall and hanging wall is mainly dependent on the degree of development and characteristics of the discontinuities. In light of the relationship between the development characteristics of the discontinuities and location of the caved zone, the rock masses in the hanging wall are mainly subjected to toppling failure. However, as we have shown in the analysis above, the rock masses in the footwall undergo failure via a mechanism that involves sliding along discontinuity surfaces as well as toppling failure. This is the main reason



there are significant differences between the movement characteristics currently observed in the ground of the footwall and those observed in the hanging wall.

According to the above analysis, the HD/VD ratio is different in different mining-affected areas and, in general, the ratio gradually increases as the distance from the mined voids increases. Hence, the proportion of the amount of toppling displacement (mainly horizontal displacement) in the total displacement (including the horizontal and vertical displacements) gradually increases as one moves further away from the boundary of the mined voids. Conversely, the proportion of the amount of the sliding displacement (mainly vertical displacement) gradually decreases. In other words, sliding failure mainly occurs in the area near the mined-out areas, and toppling failure mainly occurs in areas further away from the mined-out areas.

In the inner area close to the major crack, the current situation is that the rock mass is beginning to globally slide and topple towards the mined-out areas along the sliding surface. However, in the areas outside the major crack (e.g., the areas featuring small cracks), the rock masses are also undergoing sliding and toppling failure but on a local and not global scale. In addition, the monitoring points in the sliding–toppling area feature two onset points in their displacement–time curves corresponding to rapid increases in displacement. As the second onset points are quite obvious, the times corresponding to these points can be used to determine the times at which sliding surfaces are formed in the rock masses. Hence, global sliding surfaces can be considered to have been formed in the rock mass when the displacement shows obvious signs of rapid increase.

The waste rock mass in the caved zone resists the movement of the rock mass in the sliding–toppling area so there are no sudden and catastrophic surges in displacement, i.e., the rock mass slowly and globally slides and topples towards the mined voids (along the sliding surface). The deformation rate in the sliding–toppling area mainly depends, therefore, on the volume of the underground orebody excavated. As the orebody is excavated out, the caved waste rock above the mined-out area moves downwards into the newly mined-out area. This reduces the lateral support provided to the rock masses in the sliding–toppling area. Hence, these rock masses begin to slide and topple towards the mined voids more rapidly, i.e., the deformation rate of the rock mass in the sliding–toppling area begins to increase. The greater the volume of orebody excavated, the more significant the increase in the deformation rate of the rock masses.

The collapsed area can be backfilled to slow down the movement and reduce deformation of the rock masses surrounding the mined-out area. The thickness of the caved zone increases after the collapsed area is backfilled which increases the lateral support provided to the rock masses

surrounding the mined-out area. This is especially important for the shallow column-shaped rock masses close to the collapsed area as their fronts are free faces before the collapsed area is backfilled. When the fronts of these shallow rock masses are free faces, the degree of the toppling failure experienced by these rock masses will increase, i.e., the degree of the toppling in these rock masses will be larger than that in the rock masses in deeper parts or slightly further away from the collapsed area. This is why the HD/VD ratio at monitoring point B13 (close to the collapsed area) is larger than that at monitoring point C37 (slightly further away from the collapsing area).

When the caving of the overburden strata above the mined-out area propagates to the ground surface, the deformation and movement of the rock masses surrounding the collapsed area are affected significantly. At that moment, the rock masses surrounding the collapsed area are subjected to large-scale unloading and the deformation rate of the rock masses begins to rapidly increase. As a result, a sliding surface is formed. The mechanism and scope of the ground movement induced in a metal mine by underground orebody excavation is usually determined by the combined effect of discontinuities, bedding surfaces, faults and in situ stresses acting in that particular mine. In general, the geological conditions occurring in any two metal mines are not exactly identical. Therefore, predicting the scope of the ground movement to be expected in a metal mine by analogy may well lead to significant differences being encountered in the scope found in practice. Hence, such predictions should fully take into account the geological conditions in the mine and the possible failure mechanisms that are likely to occur (including the sliding–toppling mechanism proposed in this study).

## Conclusions

This study is based on in situ monitoring data collected at the Jinshandian Iron Mine in China over an eight-year period. The horizontal and vertical deformations of the ground were recorded and analyzed to investigate the pattern of ground movement induced by mining activity. The following results can be concluded:

- (1) The surface of the ground above and close to the mined-out voids undergoes a displacement that shows one or two obvious points that mark the onset of rapid increases in displacement (most apparent in displacement–time diagrams derived from the monitoring data). When an onset point is particularly obvious, it can be considered to correspond to the formation of a sliding surface in the rock mass surrounding the mined voids. If there is only one obvious onset point, the deforma-

tion of the ground can be split into two distinctive stages corresponding to stable and rapid deformation. If there are two obvious onset points in the displacement–time curve, the ground surface exhibits three distinctive behavioral patterns corresponding to stable, rapid and ‘even faster’ deformation.

- (2) The scope of the ground movement in the footwall is found to be significantly larger than that in the hanging wall. As a result, the rock masses in the footwall that surround the mined voids are subjected to large-scale ground movement earlier than expected. This can be attributed to the occurrence of sliding–toppling failure in the rock masses which occurs in the footwall under the combined effect of the in situ horizontal stress and high dip angle of the discontinuities. That is, the mechanism causing the rock mass in the footwall to fail not only involves toppling but also the sliding of the rock mass along a discontinuity surface. Primarily, the presence of discontinuities in the surrounding rock masses determines the large-scale ground movement observed in the footwall. They also determine the failure mode occurring. The in situ horizontal stress is, in fact, the dominant tractive force that drives the ground to move rapidly outwards.
- (3) The rock masses surrounding the mined voids mainly undergo horizontal displacement. As one moves further away from the boundary of the mined voids, the horizontal: vertical displacement ratio generally increases. The HD/VD ratio is mainly governed by the amount of displacement that can be ascribed to toppling (main cause of horizontal displacement) as the rock masses surrounding the mined voids undergo sliding–toppling failure (it increases as the degree of toppling increases). Currently, the rock masses near the mined voids are beginning to slide and topple towards the mined voids along the sliding surface globally. However, outside this sliding–toppling area, sliding and toppling failure is still occurring in the rock masses but such behavior is occurring on a local and not global scale.
- (4) The caving of the overburden strata has a significant effect on the deformation and movement of the rock masses surrounding the collapsed area when it reaches the surface of the ground. At that point in time, these rock masses are subjected to large-scale unloading. In response, the deformation rate of the rock masses increases rapidly and a sliding surface is formed. Thus, the mechanism and scope of the ground movement induced by the excavation of the underground orebodies in a metal mine are usually determined by the combined effect of the discontinuities, bedding surfaces, faults and in situ stresses acting in the mine. The geological conditions in any two metal mines will, in general, not be identical. Therefore, if the scope of

the ground movement to be expected in a metal mine is predicted using a method of analogy, it is likely that a significantly different scope will be encountered in practice. Hence, the geological conditions and possible failure mechanisms that could be encountered in the mine (including the sliding–toppling mechanism considered in this study) should be fully considered when determining the scope of the ground movement likely to be induced by the mining of the underground metal orebodies.

**Acknowledgements** The authors sincerely acknowledge the financial support from the Young Scholar Fund of the National Natural Science Foundation of China (Grant Nos. 11602284, 41602325, and 41202225) and the Youth Innovation Promotion Association CAS (2015271). The authors also sincerely thank their colleagues for the suggestions offered for improvements of this research.

## References

- Brady BHG, Brown ET (2006) Rock mechanics for underground mining. George Allen Unwin, London
- Bruneau G, Hudyma MR, Hadjigeorgiou J, Potvin Y (2003a) Influence of faulting on a mine shaft—a case study: part II—Numerical modeling. *Int J Rock Mech Min Sci* 40(01):113–125
- Bruneau G, Tyler DB, Hadjigeorgiou J, Potvin Y (2003b) Influence of faulting on a mine shaft—a case study: part I—Background and instrumentation. *Int J Rock Mech Min Sci* 40(01):95–111
- Brunton ID, Fraser SJ, Hodgkinson JH, Stewart PC (2010) Parameters influencing full scale sublevel caving material recovery at the Ridgeway gold mine. *Int J Rock Mech Min Sci* 47(4):647–656
- Cai M, Qiao L, Li C, Yu B, Wang S (2000) Results of in situ stress measurements and their application to mining design at five Chinese metal mines. *Int J Rock Mech Min Sci* 37(3):509–515
- Can E, Mekik C, Kuscu S, Akcin H (2013) Monitoring deformations on engineering structures in Kozlu Hard Coal Basin. *Nat Hazards* 65(3):2311–2330
- Cheng GW, Chen CX, Shen Q, Fu H, Xia KZ (2014) The mechanism of rock movement caused by underground mining in Chengchao iron. *Rock Soil Mech* 35(5):1421–1429 (in Chinese)
- Cheng GW, Chen CX, Ma TH, Liu HY, Tang CA (2017a) A case study on the strata movement mechanism and surface deformation regulation in Chengchao underground iron mine. *Rock Mech Rock Eng* 50(4):1011–1032
- Cheng GW, Ma TH, Tang CA, Liu HY, Wang SJ (2017b) A zoning model for coal mining—induced strata movement based on microseismic monitoring. *Int J Rock Mech Min Sci* 94:123–138
- Deng YY, Chen CX, Xia KZ, Pang HS, Sun CY, Yang KY, Zheng XW (2019) Investigation on the distribution characteristics of ground cracks in the Chengchao iron mine, China. *Environ Earth Sci* 78:280
- Ding K, Ma F, Guo J, Zhao H, Lu R, Liu F (2018) Investigation of the mechanism of roof caving in the Jinchuan nickel mine, China. *Rock Mech Rock Eng* 51(4):1215–1226
- Edelbro C, Sjöberg J, Malmgren L, Dahnér-Lindqvist C (2012) Prediction and follow-up of failure and fallouts in footwall drifts in the Kiirunavaara mine. *Can Geotech J* 49(5):546–559
- Hebblewhite BK (2001) Regional horizontal movements associated with longwall mining. University of New South Wales Mining Research Centre, New South Wales

- John F, Lupo JF (1997) Progressive failure of hanging wall and footwall Kiirunavaara mine, Sweden. *Int J Rock Mech Min Sci* 34(3–4):184.e1–186.e11
- Li X, Wang SJ, Liu TY, Ma FS (2004) Engineering geology, ground surface movement and fissures induced by underground mining in the Jinchuan nickel mine. *Eng Geol* 76(1):93–100
- Liu C, Zhou F, Gao JX, Wang J (2012) Some problems of GPS RTK technique application to mining subsidence monitoring. *Int J Min Sci Technol* 22(2):223–228
- Ma FS, Zhao HJ, Yuan RM, Guo J (2015) Ground movement resulting from underground backfill mining in a nickel mine (Gansu Province, China). *Nat Hazards* 77(3):1475–1490
- Mancini F, Stecchib F, Gabbianelli G (2009) GIS-based assessment of risk due to salt mining activities at Tuzla (Bosnia and Herzegovina). *Eng Geol* 109(3–4):170–182
- Ng AHM, Ge LL, Yan YG, Li XJ, Chang HC, Zhang K, Rizos C (2010) Mapping accumulated mine subsidence using small stack of SAR differential interferograms in the Southern coalfield of New South Wales, Australia. *Eng Geol* 115(1–2):1–15
- Reid P (1998) Horizontal movements around Cataract dam, Southern Coalfield. In: *Proceedings of the MSTS 4th triennial conference on buildings and structures subject to ground movement*, pp 157–170
- Singh UK, Stephansson OJ, Herdacia A (1993) Simulation of progressive failure in hanging-wall and footwall for mining with sub-level caving. *Trans Inst Min Metall A* 102:A188–A194
- Song X, Chen C, Xia K, Yang K, Chen S, Liu X (2018) Analysis of the surface deformation characteristics and strata movement mechanism in the main shaft area of Chengchao Iron Mine. *Environ Earth Sci* 77:335
- Svartsjaern M, Saiang D, Nordlund E, Eitzenberger A (2016) Conceptual numerical modeling of large-scale footwall behavior at the Kiirunavaara mine, and implications for deformation monitoring. *Rock Mech Rock Eng* 49(3):943–960
- Tan W, Kulatilake PHSW, Sun H (2014) Influence of an inclined rock stratum on in situ stress state in an open-pit mine. *Geotech Geol Eng* 32(1):31–42
- Villegas T, Nordlund E (2012) Time-dependent movements of the hangingwall at the Kiirunavaara mine. *Int J Min Reclam Environ* 26(2):119–133
- Villegas T, Nordlund E, Dahner-Lindqvist C (2011) Hangingwall surface subsidence at the Kiirunavaara mine, Sweden. *Eng Geol* 121(01):18–27
- Villegas T, Fernando T, Nordlund E (2013) Numerical analyses of the hangingwall failure due to sublevel caving: study case. *Int J Min Miner Eng* 4(3):201–223
- Wang F, Jiang BY, Chen SJ, Ren MZ (2019) Surface collapse control under thick unconsolidated layers by backfilling strip mining in coal mines. *Int J Rock Mech Min Sci* 113:268–277
- Xia KZ, Chen CX, Fu H, Pan YC, Deng YY (2016) Mining-induced ground deformation in tectonic stress metal mines: a case study. *Eng Geol* 210:212–230
- Xia KZ, Chen CX, Liu XM, Zheng Y, Fu H (2017) Ground movement mechanism in tectonic stress metal mines with steep structure planes. *J Cent South Univ* 24(9):2092–2104
- Xia KZ, Chen CX, Zheng Y, Zhang HN, Liu XM, Deng YY, Yang KY (2019) Engineering geology and ground collapse mechanism in the Chengchao iron-ore mine in China. *Eng Geol* 249:129–147
- Xu ZY (2007) *Rock mechanics*. China Water Power Press, Beijing (in Chinese)
- Zhao HJ, Ma FS, Zhang YM (2013) Monitoring and mechanisms of ground deformation and ground fissures induced by cut-and-fill mining in the Jinchuan Mine 2. China. *Environ Earth Sci* 68(7):1903–1910

**Publisher's Note** Springer Nature remains neutral with regard to jurisdictional claims in published maps and institutional affiliations.